ARTICLES
https://doi.org/10.1038/s43018-021-00203-x
nature cancer

A first-in-class polymerase theta inhibitor selectively targets homologous-recombination-deficient tumors

Jia Zhou[1], Camille Gelot[2], Constantia Pantelidou[3], Adam Li[1], Hatice Yücel[2], Rachel E. Davis[4], Anniina Färkkilä[1], Bose Kochupurakkal[1], Aleem Syed[5], Geoffrey I. Shapiro[3,6], John A. Tainer[5], Brian S. J. Blagg[4], Raphael Ceccaldi[2,8] ✉ and Alan D. D'Andrea[1,6,7,8] ✉

DNA polymerase theta (POLθ or POLQ) is synthetic lethal with homologous recombination (HR) deficiency and is thus a candidate target for HR-deficient cancers. Through high-throughput small-molecule screens, we identified the antibiotic novobiocin (NVB) as a specific POLθ inhibitor that selectively kills HR-deficient tumor cells in vitro and in vivo. NVB directly binds to the POLθ ATPase domain, inhibits its ATPase activity and phenocopies POLθ depletion. NVB kills HR-deficient breast and ovarian tumors in genetically engineered mouse models and xenograft and patient-derived xenograft models. Increased POLθ levels predict NVB sensitivity, and HR-deficient tumor cells with acquired resistance to poly(ADP-ribose) polymerase (PARP) inhibitors (PARPi) are sensitive to NVB in vitro and in vivo. Mechanistically, NVB-mediated cell death in PARPi-resistant cells arises from increased double-strand break end resection, leading to accumulation of single-stranded DNA intermediates and non-functional foci of the recombinase RAD51. Our results demonstrate that NVB may be useful alone or in combination with PARPi for treating HR-deficient tumors, including those with acquired PARPi resistance.

Deficiency of HR-mediated DNA repair occurs mainly through genetic or epigenetic inactivation of the *BRCA1* and *BRCA2* (*BRCA1/2*) genes, and it plays a role in the initiation and progression of many tumor types[1]. HR deficiency also provides unique opportunities for targeted therapy, as exemplified by the extreme sensitivity of *BRCA1/2*-mutated tumors to PARPi[2,3]. In the last decade, several PARPi were approved for clinical use. At first, PARPi were solely used in combination with chemotherapeutics, and platinum sensitivity was used as a surrogate marker of HR deficiency for enrolling patients for treatment[4]. The promising clinical response of patients with germline *BRCA1/2* mutations prompted the use of PARPi for patients with somatic *BRCA1/2* mutations as well. In addition, it also opened up the possibility for extended use of PARPi for the treatment of various types of ovarian, breast, pancreatic and prostate tumors with HR defects[1]. PARPi efficacy is currently being evaluated in different clinical settings such as first-line chemotherapy, neoadjuvant therapy (that is, before chemotherapy) and combination therapy with chemo- or immunotherapies[1,5–8].

Despite initial sensitivity to PARPi, resistance to these drugs is emerging as the major obstacle to their clinical effectiveness in patients with HR-deficient tumors[9]. In addition, resistance to PARPi often correlates with platinum resistance, which remains the backbone therapy for most *BRCA1/2*-mutated tumors. The absence of alternative therapeutic options for patients with tumors with innate or acquired resistance underlines the urgency to develop additional therapeutics. While several mechanisms of PARPi resistance have been described[10–13], an effective method for overcoming such resistance is still lacking.

POLθ recently emerged as a new promising drug target for the treatment of HR-deficient tumors. POLθ expression is particularly high in subtypes of breast and ovarian tumors with defects in HR[14], where it mediates backup DNA double-strand break (DSB) repair, compensating for the loss of HR[15]. As a result, POLθ is synthetic lethal with HR, and POLθ inhibition in HR-deficient tumors induces cell death[14,16]. In addition, POLθ depletion synergizes with PARPi in the killing of HR-deficient tumors[14,16].

Synthetic lethality between HR deficiency and POLθ inhibition hinges on several functions that POLθ exhibits in maintaining genomic stability and preventing tumorigenesis[17]. POLθ was first described as a translesion DNA polymerase (TLS)[18], and this activity was recently shown to prevent the onset of skin cancer[19]. POLθ is also a crucial enzyme in the mutagenic microhomology-mediated end-joining (MMEJ) repair of DSBs[20], a pathway that plays critical role in genomic stability[21]. Inhibiting PARP1, a key enzyme in MMEJ[22], prevents POLθ recruitment to sites of laser micro-irradiation[14,16]. Because POLθ depletion and PARPi have additive effects on HR-deficient cells, these data suggest that functions of POLθ outside PARP-mediated MMEJ are also key to the survival of HR-deficient cells.

POLθ is a large protein that contains three domains and is structurally and functionally distinct from other polymerases[17,23]. The N terminus contains a helicase-like ATPase domain that can unwind several types of DNA structures[24], while the central domain binds

---

[1]Department of Radiation Oncology, Dana-Farber Cancer Institute, Harvard Medical School, Boston, MA, USA. [2]Inserm U830, PSL Research University, Institut Curie, Paris, France. [3]Department of Medical Oncology, Dana-Farber Cancer Institute and Department of Medicine, Harvard Medical School, Boston, MA, USA. [4]Department of Chemistry and Biochemistry, University of Notre Dame, Notre Dame, IN, USA. [5]Departments of Cancer Biology and Molecular and Cellular Oncology, University of Texas MD Anderson Cancer Center, Houston, TX, USA. [6]Center for DNA Damage and Repair, Dana-Farber Cancer Institute, Boston, MA, USA. [7]Susan F. Smith Center for Women's Cancers, Dana-Farber Cancer Institute, Boston, MA, USA. [8]These authors jointly supervised this work: Raphael Ceccaldi, Alan D. D'Andrea. ✉e-mail: raphael.ceccaldi@curie.fr; alan_dandrea@dfci.harvard.edu

RAD51, displaces replication protein A (RPA) from resected DSBs and antagonizes HR repair in an ATP-hydrolysis dependent manner[14,16,25]. Finally, the C terminus contains a nuclease domain that trims DNA ends and a polymerase domain that fills in nucleotides during MMEJ[26]. Both ATPase and polymerase domains are required for MMEJ repair[27].

POLθ has several functions that preserve genomic stability, and POLθ-mediated MMEJ repair can compensate for the loss of HR[15]. It remains unclear which of the many functions of POLθ underlie synthetic lethality with HR. Nevertheless, POLθ exhibits unique features of druggability, providing a strong rationale for developing POLθ inhibitors[4,28].

Here, we performed a small-molecule screen for inhibitors of POLθ ATPase activity and identified the antibiotic NVB as a specific and potent inhibitor of human POLθ. NVB binds to purified POLθ protein, prevents its recruitment to DNA damage and inhibits MMEJ repair. Importantly, we show that NVB selectively kills HR-deficient (BRCA1- and BRCA2-deficient) cells over wild-type (WT) cells and potentiates the cytotoxic effect of PARPi in HR-deficient tumor cells in vitro and in vivo. Moreover, NVB also kills HR-deficient, PARPi-resistant tumor cells. Our results demonstrate that NVB can be used alone or in combination with PARPi for treating HR-deficient tumors, even after they acquire PARPi resistance.

Results

A small-molecule screen identifies NVB as a specific POLθ inhibitor. The ATPase activity of POLθ is required for the survival of HR-deficient cells[14]. We took advantage of the strong ATPase activity of purified POLθ in vitro (Extended Data Fig. 1a) and performed a large-scale small-molecule screen to identify POLθ inhibitors based on the ADP-Glo luminescent assay (Fig. 1a,b). We screened a total of 23,513 small molecules across multiple libraries (enriched with known bioactive compounds, Supplementary Tables 1 and 2) in duplicate and identified 72 compounds that significantly (Z score < -4) reduced POLθ ATPase activity (Fig. 1b and Supplementary Table 3). These compounds account for only 0.3% of the total small molecules screened, arguing for a low rate of false-positive hits. A secondary screen using the 72 initial hits was performed in the presence and absence of single-stranded (ss)DNA to confirm the initial screen results and to exclude compounds that directly interact with ssDNA (Extended Data Fig. 1b). Among the 72 small molecules, ten hits were identified that inhibited POLθ ATPase activity more than 50% both with and without ssDNA (≤15% difference in inhibition) (Supplementary Table 4). Aurintricarboxylic acid, reactive blue 2, suramin, and NVB were the four most potent POLθ inhibitors.

These top hits were individually verified in a ^{32}P-based radiometric ATPase assay with POLθ and another known DNA repair-related ATPase, SMARCAL1 (ref. [29]). Only NVB showed high specific inhibition of POLθ with little effect on SMARCAL1, while other compounds inhibited both ATPases (Extended Data Fig. 1c). We thus focused our future studies on NVB. Next, we performed a dose–response experiment of NVB on POLθ ATPase activity using the ADP-Glo assay, along with six other DNA repair-related enzymes, heat shock protein 90 alpha family class A member 1 (HSP90AA1), thyroid receptor interacting protein 13 (TRIP13), helicase BLM, RAD51, SMARCAL1 and chromodomain helicase DNA-binding protein 1 (CHD1) (Fig. 1c and Extended Data Fig. 1d). NVB inhibited POLθ with a half-maximum inhibitory concentration (IC_{50}) of 24 µM, but it did not significantly inhibit other ATPases, supporting the specific inhibition of POLθ by NVB.

To further evaluate the specificity of NVB for POLθ, we analyzed its binding capacity. NVB-conjugated beads pulled down the purified ATPase domain of POLθ but not purified SMARCAL1, CHD1, BLM or RAD51, suggesting that NVB directly and specifically binds to the POLθ ATPase domain in vitro (Extended Data Fig. 1d–f). NVB-conjugated beads also pulled down POLθ–GFP expressed in cells, and this binding was competed by free NVB (Extended Data Fig. 1g,h). Thermal shift assays using cell lysate of GFP–POLθ-expressing HEK293T cells showed that NVB stabilized GFP–POLθ (Extended Data Fig. 1i). Thermal shift assays with the purified POLθ ATPase domain showed that NVB increased POLθ stability in a dose-dependent manner, further suggesting a direct ligand–protein binding of NVB to POLθ (Extended Data Fig. 1j). As controls, NVB did not increase the thermal stability of BLM or meiotic recombination 11 homolog A (MRE11) (Extended Data Fig. 1k,l). Finally, we performed molecular docking to identify the NVB-binding site using the published crystal structure of the POLθ ATPase domain[30]. Computational docking results revealed a deep tunnel within the POLθ ATPase domain that could accommodate NVB, which is located next to the ATP-binding pocket (Fig. 1d). In sum, these data demonstrate that NVB binds directly and specifically to the POLθ ATPase domain in vitro.

We next assessed whether cellular exposure to NVB has the same consequences as POLθ depletion. Both the ATPase and the

Fig. 1 | A small-molecule screen identifies NVB as a specific POLθ ATPase inhibitor that kills HR-deficient tumors. a, Domain structures of full-length (FL) POLθ and the ATPase domain (ΔPol, amino acids 1–987) of POLθ, a Coomassie-stained gel of the purified POLθ ATPase domain used for the screen and a schematic of the small-molecule screen. **b**, Results of the small-molecule screen. Shown is POLθ ATPase activity in the presence of small-molecule libraries (enriched with bioactive compounds). The four top hits verified in the secondary screen (Extended Data Fig. 1b) are labeled: reactive blue 2 (RB), suramin (SUR), NVB and aurintricarboxylic acid (ATA). Data are means from $n = 2$ replicates. **c**, Quantification of the ATPase activity of POLθ, SMARCAL1, CHD1, BLM, TRIP13, RAD51 and HSP90AA1 with increasing concentrations of NVB. ATPase activity was determined by the ADP-Glo assay (Promega). Activities were normalized to values from the DMSO (0.1%) control. Means of six replicates from $n = 2$ independent experiments are shown. **d**, The NVB-binding tunnel in the POLθ ATPase domain (shown in surface, Protein Data Bank (PDB) 5AGA) was predicted by extra-precision glide docking and lowest binding free energy from prime molecular mechanics with generalized Born and surface area approximation (MM-GBSA) calculations to have multiple hydrogen bonds and close hydrophobic packing. Top and side views showing NVB docking into the tunnel. Binding modes of NVB (green sticks) and adenylyl-imidodiphosphate (AMP-PNP) (magenta sticks) in the POLθ helicase domain (PDB 5AGA) with the green sphere showing the active-site Mg^{2+} ion. **e**, Quantification and representative images of POLθ-GFP accumulation at sites of laser micro-irradiated DNA damage in RPE1 *POLQ*$^{-/-}$ cells overexpressing GFP-tagged WT POLQ, polymerase (Pol)-mutant POLQ, ATPase (helicase)-mutant POLQ or double-mutant POLQ. GFP-POLQ-WT-expressing cells treated with DMSO (0.1%) or 100 µM NVB are shown. Mean ± s.e.m. are shown. WT (+DMSO), $n = 7$ cells; WT (+NVB), $n = 8$ cells; polymerase dead, $n = 24$ cells; ATPase dead, $n = 13$ cells; polymerase and ATPase dead, $n = 14$ cells from three independent experiments. GFP only, $n = 4$ from two independent experiments. **f**, MMEJ and HR repair reporter assays in U2OS cells treated with increasing concentrations of NVB. Percentage of GFP-positive cells are shown as pathway efficiency. Mean ± s.d. from $n = 6$ (for MMEJ) and $n = 3$ (for HR) measurements from three independent experiments, ordinary one-way ANOVA. NS, not significant. **g**, Tumor growth in the GEMM model (*Brca1*$^{-/-}$ triple-negative breast cancer) after treatment with vehicle (PBS) or NVB. Tumor-bearing FVB/129P2 mice were treated with PBS or 100 mg per kg NVB via intraperitoneal (i.p.) injection twice a day for 5 weeks. Mean ± s.e.m. are shown, $n = 6$ mice for the PBS group and $n = 7$ mice for the NVB group. **h**, Survival plot of the experiment shown in **g**. Median survival and a P value are shown. Statistical analyses in **g**,**h** are two-tailed t-tests. $^{*}P < 0.05$, $^{**}P < 0.01$.

polymerase domains contribute to efficient MMEJ repair activity[27], and PARP-dependent recruitment of POLθ to DSB sites is a crucial step in this function[14,16]. Phenocopying the ATPase mutant of POLθ, inhibition of POLθ by NVB prevented the recruitment of POLθ to laser micro-irradiated DNA-damage sites in human cells (Fig. 1e). Consequently, NVB inhibited MMEJ activity in U2OS cells, as

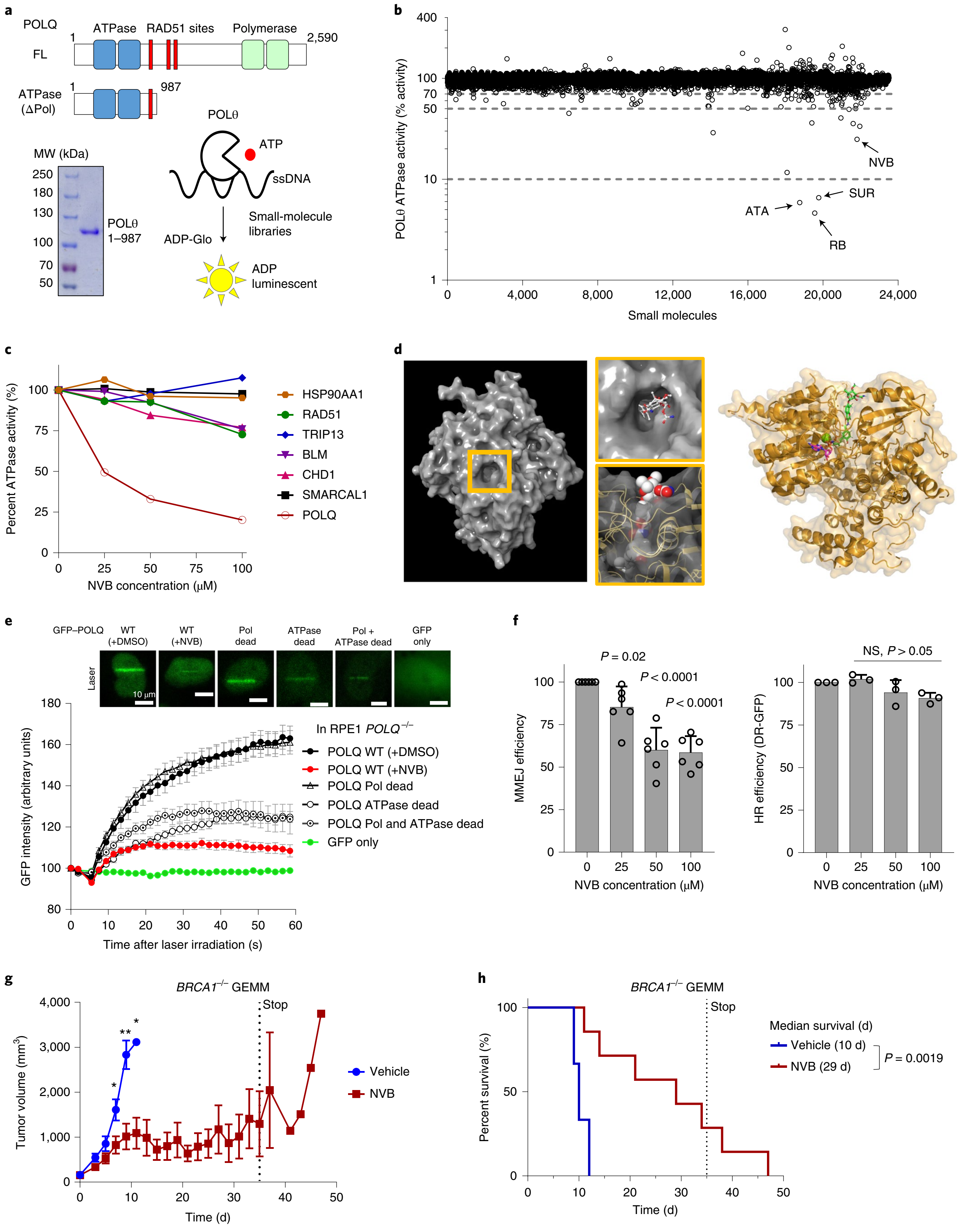

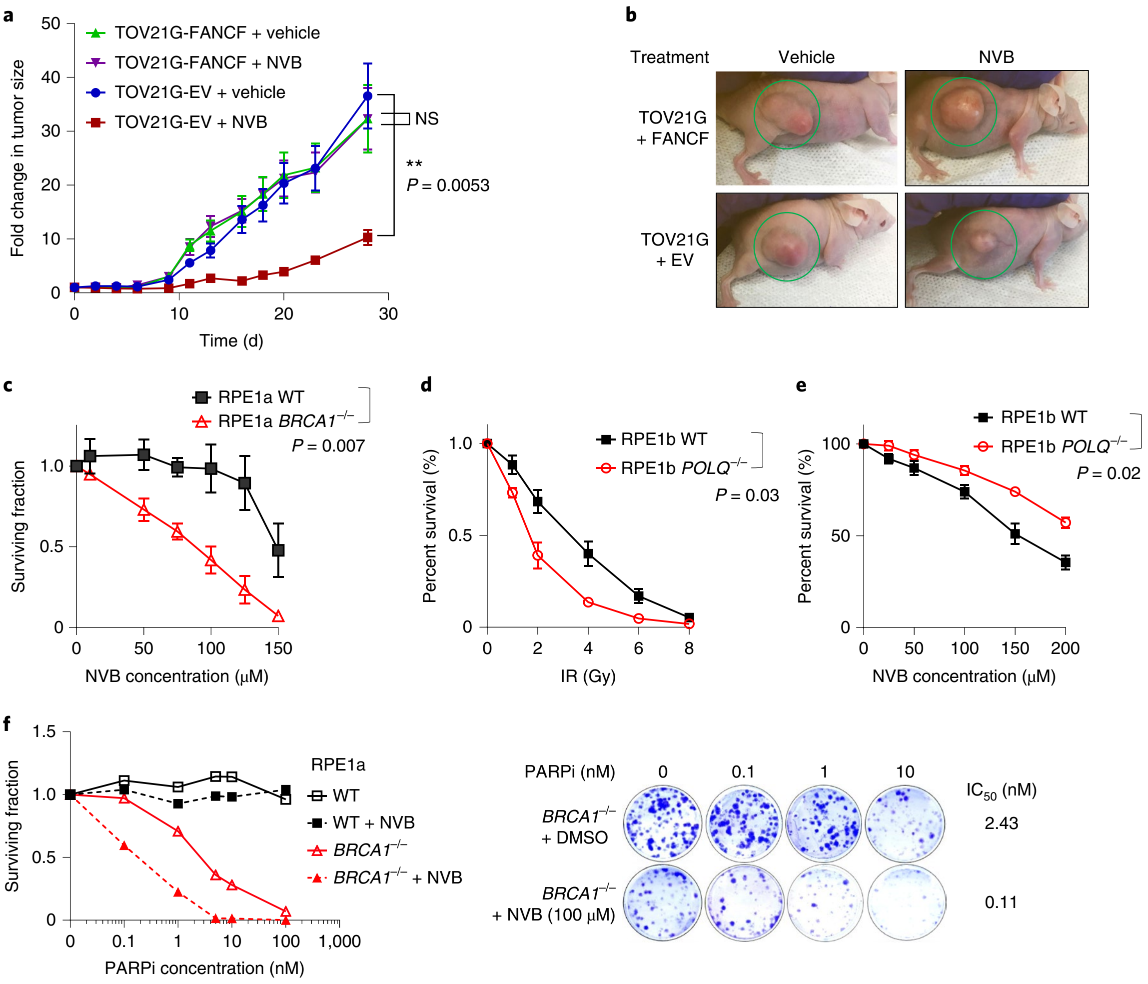

Fig. 2 | NVB kills HR-deficient tumors in vivo and in vitro and synergizes with PARPi. a, Tumor growth in the xenograft model with TOV21G (FANCF-deficient ovarian cancer) or FANCF-complemented TOV21G cells. Tumor-bearing mice were treated with vehicle or 100 mg per kg NVB via i.p. injection twice a day for 4 weeks. Fold change of tumor size was calculated using the formula fold change = $T \div T_0$, where T is the tumor size at a given time and T_0 is the initial tumor size. Data are mean ± s.e.m. from $n = 10$ mice in each group. Statistical analysis was performed by Dunn's multiple-comparisons test. EV, empty vector. **b**, Representative images of TOV21G xenograft tumors at the end of NVB treatment. **c**, Clonogenic survival of *BRCA1*$^{-/-}$ and WT RPE1 cells with increasing concentrations of the POLθ inhibitor NVB. Survival is normalized to the values from the untreated sample. Data shown are mean ± s.e.m., $n = 3$ independent experiments. **d**, IR sensitivity of WT and *POLQ*$^{-/-}$ RPE1 cells in clonogenic assays. **e**, NVB sensitivity of WT and *POLQ*$^{-/-}$ RPE1 cells. Data shown in **d**,**e** are mean ± s.d. from $n = 6$ biological replicates. Significance levels in **c**–**e** were determined by two-tailed paired t-tests. **f**, Clonogenic survival of *BRCA1*$^{-/-}$ and WT RPE1 cells with increasing concentrations of the PARPi (rucaparib) alone or in combination with NVB. Quantification of the surviving fraction (means from $n = 2$ independent experiments), representative images and calculated IC_{50} values are shown.

measured by the GFP-based alternative end joining (EJ2) reporter assay, but it had little effect on HR activity measured by the direct repeat (DR)-GFP reporter assay (Fig. 1f). POLθ also functions as an anti-recombinase that antagonizes HR, and depletion of POLθ increases RAD51 (ref. [14])- and phosphorylated histone γH2AX (ref. [31])-foci assembly. Similarly, more RAD51 foci and γH2AX foci were observed after gamma irradiation (IR) in the presence of NVB in U2OS cells (Extended Data Fig. 2a,b), although the effect was not as strong as previously reported with small interfering RNA POLθ knockdown[14]. In sum, these results establish that NVB-mediated POLθ inhibition impairs the DNA repair function of POLθ and phenocopies POLθ depletion in human cells.

NVB specifically kills HR-deficient tumors. NVB is a safe drug and has already been used in anti-cancer trials, although treated patients were not preselected to have HR-deficient cancers[32–35]. As depletion of POLθ is synthetically lethal in HR-deficient tumor cells[14,16], we next directly tested whether NVB can kill HR-deficient tumor cells in animal models. First, we evaluated the efficacy of NVB in tumors derived from the K14-Cre-*Brca1*$^{f/f}$;*Trp53*$^{f/f}$ genetically engineered mouse model (GEMM) of triple-negative breast cancer[36,37]. Tumors from this model were transplanted into immunocompetent FVB/129P2 syngeneic mice that were subsequently treated with NVB. NVB strongly suppressed the growth of these BRCA1-deficient GEMM-derived tumors (Fig. 1g and Extended Data Fig. 3a). NVB-treated tumors were significantly smaller than those from vehicle-treated mice after 7 d of treatment and beyond. NVB treatment prolonged the overall survival of tumor-bearing mice by threefold compared to vehicle treatment, with median survival times of 29 and 10 d for NVB- and vehicle-treated mice, respectively (Fig. 1h).

Next, we tested whether the efficacy of NVB in vivo was specific to HR-deficient tumors. FA complementation group F (FANCF)-deficient TOV21G cells are human ovarian cancer cells with reduced HR capacity, which grow well as tumor xenografts in mice[38,39]. We thus performed a mouse xenograft

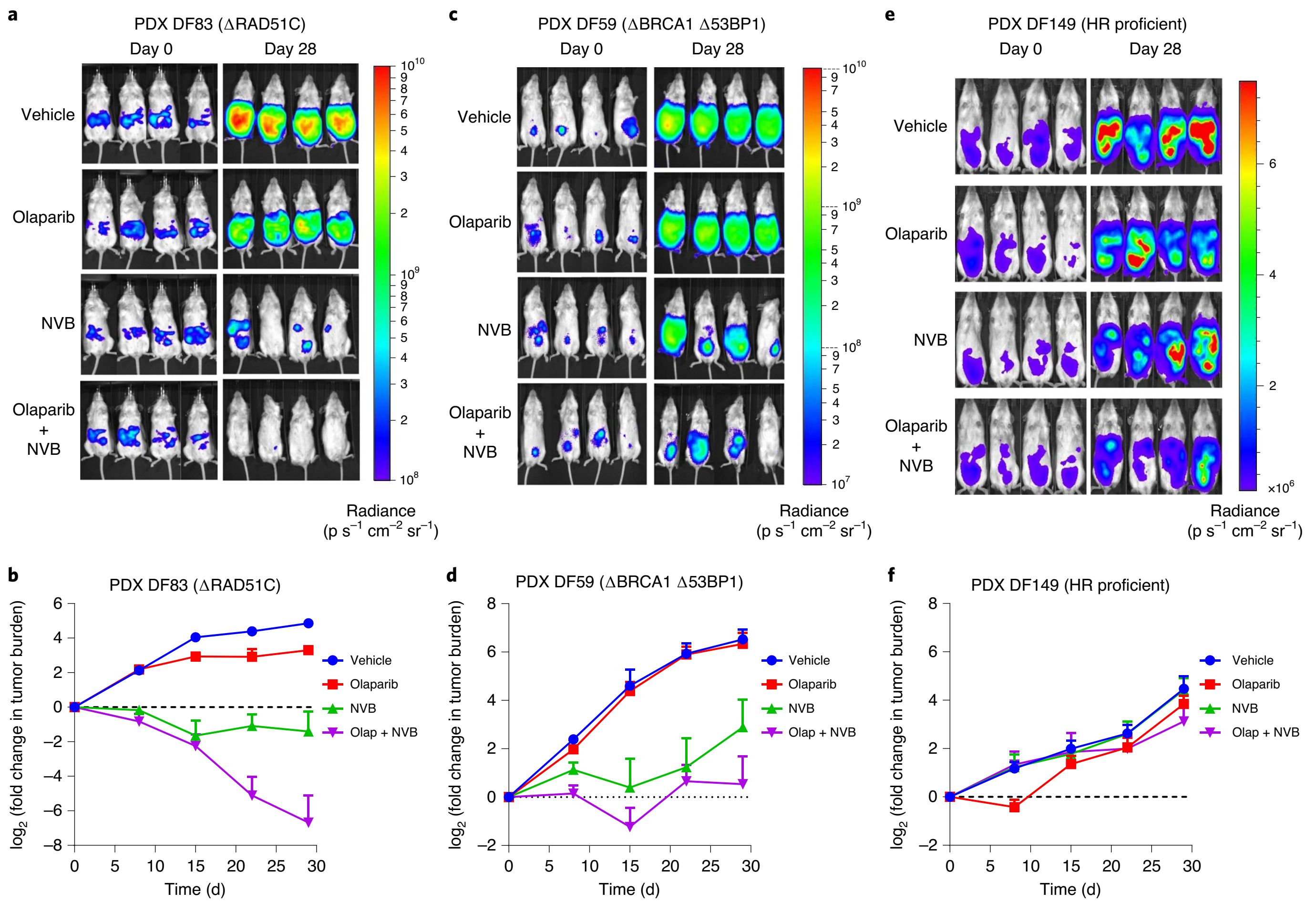

Fig. 3 | NVB kills HR-deficient tumors and overrides PARPi resistance in vivo in PDX models. a,**b**, Efficacy of NVB in the PDX model DF83 (RAD51C deficient). NSG mice ($n=7$ mice per group) bearing luciferized DF83 cells derived from a patient with ovarian cancer were treated with 50 mg per kg olaparib (daily, orally), 75 mg per kg NVB (i.p., twice daily) or both for 4 weeks. Tumor growth was monitored weekly by BLI (p, photons). Representative images of tumor burden on day 0 and day 28 are shown, and quantifications shown are mean ± s.e.m. for $n=8$ mice. $\log_2$ (fold change in tumor size) values were calculated using the formula $\log_2(T \div T_0)$, where T is the tumor volume at a given time and T_0 is the initial tumor volume. **c**,**d**, Efficacy of NVB in the PARPi-resistant PDX model DF59 (BRCA1-deficient with 53BP1 loss), $n=6$ mice per group. The same conditions and analysis were applied as described in **a**,**b**. Olap, olaparib. **e**,**f**, Efficacy of NVB in the PARPi-resistant PDX model DF149 (WT BRCA1, HR proficient), $n=7$ mice per group. The same conditions and analysis were applied as described in **a**,**b**.

study with FANCF-deficient (TOV21G with empty vector) and FANCF-complemented (TOV21G with *FANCF* cDNA) cell lines (Fig. 2a,b). In vitro, TOV21G cells with empty vector but not TOV21G cells complemented with *FANCF* cDNA were sensitive to olaparib and NVB (Extended Data Fig. 3b,c)[39]. In vivo, while vehicle treatment had no impact on the growth of FANCF-deficient or FANCF-complemented tumors, NVB specifically impaired the growth of FANCF-deficient tumors, with no effect on FANCF-complemented tumors (Fig. 2a,b). We also measured RAD51 foci as a pharmacodynamic biomarker and showed that RAD51 foci were strongly induced in treated tumors (Extended Data Fig. 3d–f). These results demonstrate that NVB strongly and specifically suppresses the growth of HR-deficient tumors in vivo.

To confirm and strengthen the in vivo results, we studied isogenic pairs of HR-deficient and HR-proficient cells in vitro. We generated *BRCA1*- and *BRCA2*-knockout RPE1 cells (referred to as *BRCA1*$^{-/-}$ and *BRCA2*$^{-/-}$) in a *TP53*$^{-/-}$ background, which were sensitive to PARPi (Extended Data Fig. 4a,b). Consistent with our in vivo data, clonogenic survival assays showed that NVB significantly reduced the survival of *BRCA1*$^{-/-}$ and *BRCA2*$^{-/-}$ cells, compared to isogenic WT cells (Fig. 2c and Extended Data Fig. 4c). We also tested the top initial hits from our screen for their ability to differentially affect the survival of *BRCA1*$^{-/-}$ and WT cells. Among these, NVB had the highest efficacy in selectively killing *BRCA1*$^{-/-}$ cells (Extended Data Fig. 4d).

To demonstrate the cellular outcome of NVB exposure, we next showed that NVB exposure induces apoptosis in *BRCA1*$^{-/-}$ but not WT cells in a dose-dependent manner (Extended Data Fig. 5a). NVB induced chromosomal aberrations and radial chromosomes (a marker of genomic instability) in *BRCA1*$^{-/-}$ cells, even in the absence of the cross-linking agent mitomycin C (Extended Data Fig. 5b–d), confirming that NVB increases DNA damage. These results further demonstrate that NVB phenocopies POLθ depletion, and they indicate that NVB-mediated POLθ inhibition is synthetically lethal with HR deficiency and specifically induces cell death in HR-deficient tumor cells.

POLθ is the major target of NVB in human cells. Off-target effects are major concerns of biological small inhibitors. To further evaluate whether POLθ is the specific target of NVB and to demonstrate the specificity of NVB in cells, we knocked out the *POLQ* gene in RPE1 cells using CRISPR–Cas9 and asked whether the loss of

POLQ alleviates the cytotoxicity of NVB. *POLQ*-knockout cells were confirmed by genomic sequencing and their increased sensitivity to irradiation (Fig. 2d). Importantly, RPE1 $POLQ^{-/-}$ cells showed higher tolerance to NVB than WT cells (Fig. 2e). In addition, $POLQ^{-/-}$ U2OS cells were also more resistant to NVB than WT cells (Extended Data Fig. 6a–e). These data indicate that POLθ is a major target of NVB in human cells.

NVB is a known coumarin antibiotic that inhibits DNA gyrase in bacteria[40]. NVB was reported to inhibit the ATPase of HSP90 and that of the DNA gyrase homolog topoisomerase II (TOP2) in eukaryotes[41,42], suggesting that these enzymes may be off-target enzymes of NVB. However, other reports suggest that NVB does not inhibit TOP2 in eukaryotic cells[43]. Additionally, reported IC_{50} values of these targets are very high (approximately 700 µM for HSP90 and 300 µM for TOP2), compared with the IC_{50} of POLθ (24 µM by the ATPase inhibition assay, Fig. 1c). Nevertheless, we next examined whether the cytotoxic effect of NVB in HR-deficient cells resulted from off-target inhibition of HSP90 or TOP2. Unlike the well-characterized HSP90 inhibitor PU-H71, NVB treatment at a concentration that killed HR-deficient cells (that is, 100 µM) did not induce the degradation of HSP90 clients, such as kinase AKT1, BRCA1 or kinase CDK6, or increase the expression of HSP70 (Extended Data Fig. 7a–c). These results suggest that the cytotoxic effect of NVB is not related to HSP90 inhibition. Furthermore, the combination of NVB and the TOP2 inhibitor etoposide exhibited additive cytotoxicity in TOV21G and CAPAN1 cells (Extended Data Fig. 7d,e), suggesting that NVB and etoposide do not share TOP2 as a target and that NVB cytotoxicity is unrelated to TOP2 inhibition.

NVB potentiates the effect of PARPi in HR-deficient tumors. PARPi are currently being evaluated in different combination therapy settings with cytotoxic chemotherapy, radiation, targeted therapies and immunotherapies[44]. We explored whether the combination of NVB and a PARPi may be more effective than PARP inhibition alone in killing HR-deficient tumors. Indeed, NVB further sensitized $BRCA1^{-/-}$ RPE1 cells to the PARPi rucaparib but not BRCA-proficient WT cells in clonogenic assays (Fig. 2f). We studied the combination with a second PARPi, olaparib, for which synergism of NVB and olaparib was also observed in HR-deficient TOV21G cells with empty vector but not in HR-proficient FANCF-complemented TOV21G cells (Extended Data Fig. 7f). Importantly, NVB reduced the IC_{50} of rucaparib by more than 20-fold in $BRCA1^{-/-}$ RPE1 cells and the IC_{50} of olaparib by more than 40-fold in TOV21G cells compared to their respective HR-proficient counterparts (Fig. 2f and Extended Data Fig. 7g). One strategy to prevent acquired resistance during treatment is combination therapy. The observed synergy between NVB and PARPi prompted us to evaluate whether NVB could overcome PARPi resistance in HR-deficient tumors.

POLθ inhibition by NVB overcomes acquired PARPi resistance. Multiple PARPi, including olaparib, niraparib, rucaparib and talazoparib, have received approval for the treatment of ovarian and breast tumors with HR deficiency[45]. Despite the remarkable initial tumor response and improved progression-free survival in patients with HR deficiency[5–8], acquired PARPi resistance is emerging as an unmet medical need[9].

To evaluate whether POLθ inhibition could represent a new therapeutic option for PARPi-resistant tumors, we first tested the efficacy in vivo of NVB in the patient-derived xenograft (PDX) model DF83, generated from an HR-deficient (loss of RAD51C expression), human high-grade serous ovarian carcinoma[46]. NOD SCID gamma (NSG) mice bearing tumors of the HR-deficient DF83 ovarian cancer PDX model were treated with olaparib, NVB or a combination of the two, and tumor growth was monitored by bioluminescence imaging (BLI) (Fig. 3a). To determine the combined effect with NVB, olaparib was delivered at a submaximal dose (50 mg per kg daily), and we observed only a small degree of tumor growth inhibition. Treatment of DF83 with NVB alone (75 mg per kg, twice a day) led to tumor regression, while tumors in vehicle-treated mice showed exponential growth (Fig. 3b). Strikingly, when DF83-tumor-bearing mice were given NVB and olaparib in combination, we observed complete tumor regression, and few tumor cells were detectable via BLI on day 28 in this group (Fig. 3a,b). These in vivo results suggest that NVB may be useful in combination with PARPi to achieve better efficacy and prevent drug resistance in HR-deficient tumors. No significant toxicity to normal mouse tissue was observed from the drug combination.

Next, we evaluated the efficacy of NVB alone and in combination with olaparib in the PARPi-resistant PDX model DF59, which was isolated from a patient with a germline *BRCA1* mutation and acquired PARPi resistance. This model harbors biallelic mutations in the *TP53BP1* locus, providing a mechanism of the acquired PARPi resistance[46]. In the DF59 PDX model, there was no response to olaparib monotherapy, but NVB monotherapy substantially reduced tumor growth, indicating a lack of cross-resistance between PARP inhibition and NVB. Importantly, the combination of NVB and olaparib further inhibited DF59 tumor growth, with tumor regression in the first 2 weeks (Fig. 3c,d). In contrast to DF83 and DF59 models, the BRCA1-WT, HR-proficient PDX model DF149 was resistant to both drugs and to the combination (Fig. 3e,f). These data demonstrate that NVB can inhibit the growth of *BRCA1*-mutated, PARPi-resistant tumors in vivo and that the combination of NVB and a PARPi is particularly effective in treating at least some PARPi-resistant tumors.

NVB induces excessive DSB end resection and RAD51 foci. We next studied the mechanism of cell killing by NVB. Previous studies demonstrated that the ATPase domain of POLθ counteracts RPA

Fig. 4 | NVB induces excessive DSB end resection and non-productive RAD51 foci. a, DSB end resection assay in U2OS cells with or without NVB. A scheme of the AsiSI resection assay is shown. Cells were incubated with 100 µM NVB for 18 h and then with 4-hydroxytamoxifen (4-OHT) for 4 h. Genomic DNA were isolated to analyze the percent of ssDNA flanking the AsiSI DSB site at indicated positions, by digestion with restriction endonuclease BrsGI and qPCR quantification. Mean ± s.e.m., $n = 3$ independent experiments, two-tailed unpaired *t*-tests. Chr., chromosome. **b**, Western blot analysis of phospho-RPA32 (p-RPA32) in samples of the DF59 PDX model, 52 h after the first dose. Tumor-bearing mice were dosed as described for the efficacy study in Fig. 3. **c**,**d**, Representative immunohistochemical images and quantification of RAD51 foci in DF59 and DF83 PDX models. Formalin-fixed, paraffin-embedded sections of the isolated tumor cells (as described in **b**) were stained with an anti-RAD51 antibody. Percentages of RAD51-foci-positive cells (>4 foci per cell) in three random ×40 fields were estimated in DF59. No RAD51 focus was observed in the DF83 model. Data shown are mean ± s.d., $n = 3$ tumors, ordinary one-way ANOVA with Bonferroni's multiple-comparisons test. **e**,**f**, CellTiter-Glo cell viability assay in parental MDA-MB-436 (*BRCA1* mutated) and PARPi-resistant MDA-MB-436-R cells with increasing concentrations of olaparib (**e**) or NVB (**f**). Mean ± s.e.m. are shown, with $n = 6$ independent cultures. Two-tailed paired *t*-test. **g**, RAD51-focus assay with DMSO or NVB in MDA-MB-436 or MDA-MB-436-R cells. Cells with more than five foci were counted as positive. Data are means from two independent experiments. **h**, A scheme shows the mechanism of NVB cytotoxicity in PARPi-naive and -resistant tumor cells. In PARPi-naive HR-deficient settings, cells rely on MMEJ to repair DSBs. NVB inhibits MMEJ repair and causes unrepaired DSBs, leading to cell death. In HR-deficient but PARPi-resistant settings, NVB inhibits the counteracting function of POLθ on RPA and RAD51, leading to enhanced DSB resection, accumulation of nonfunctional RAD51 foci, unrepaired DSBs and eventually cell death. POLQi, POLQ inhibitor.

binding at resected DSBs to facilitate their repair by MMEJ[25]. We therefore hypothesized that DSBs would be excessively resected when POLθ is inhibited. We measured DNA resection at DSBs, generated by restriction endonuclease AsiSI, in U2OS cells in the presence or absence of NVB. In this assay, DSBs were induced by 4-hydroxytamoxifen, and the percentage of ssDNA was measured

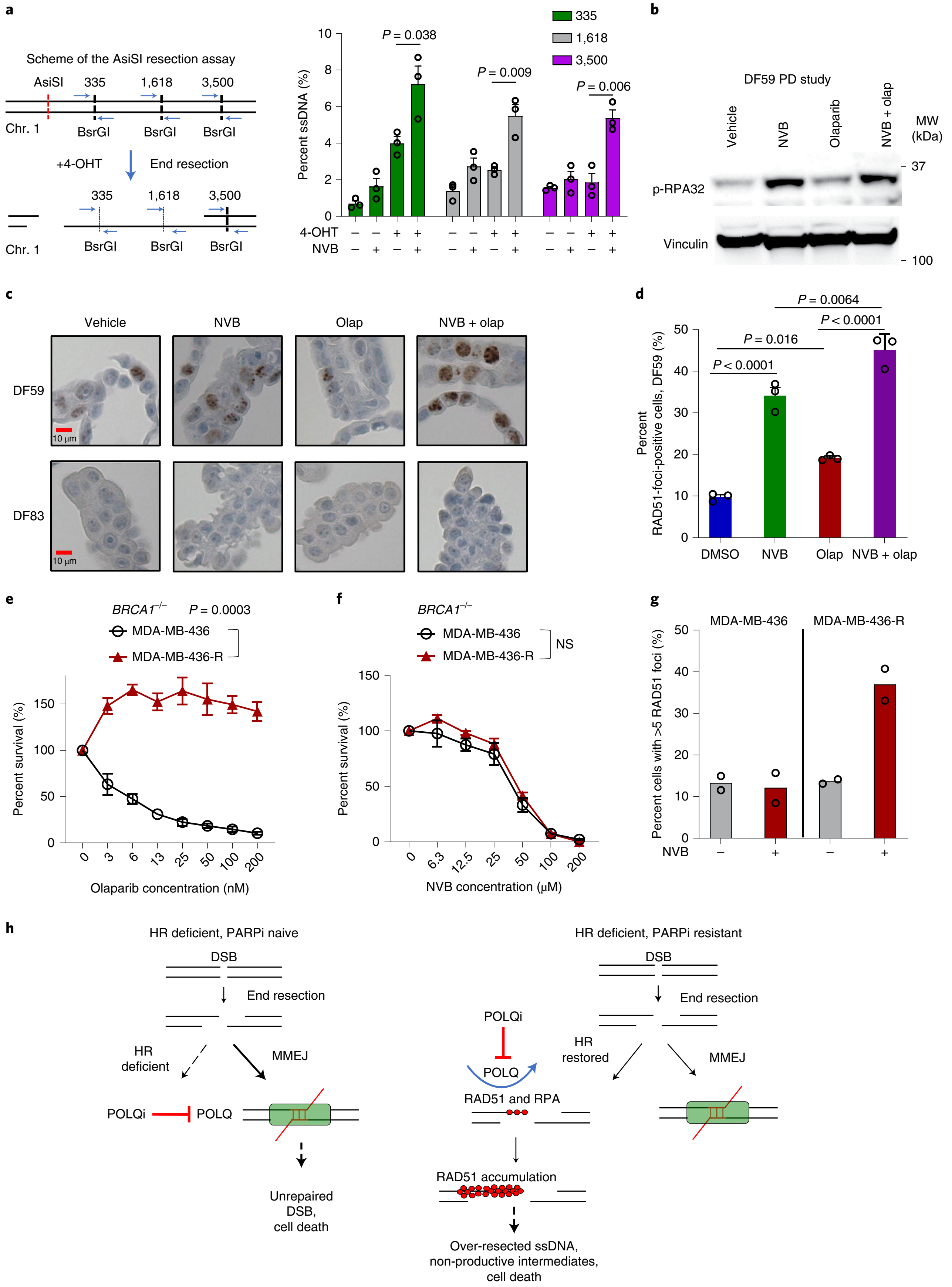

by quantitative (q)PCR[47]. The amount of ssDNA around the DSB was significantly higher when cells were treated with NVB versus DMSO (Fig. 4a). Consistent with this result, NVB-treated tumor samples from the DF59 PDX model exhibited higher levels of phospho-RPA32, a measure of ssDNA accumulation, than did vehicle-treated samples (Fig. 4b). These data suggest that POLθ inhibition by NVB can promote DSB end resection.

We previously showed that depletion of POLθ in HR-deficient tumors causes RAD51 accumulation[14], perhaps resulting from excessive DSB end resection. Similarly, tumor suppressor P53-binding protein 1 (53BP1) and POLθ are synthetic lethal, and *Trp53bp1*;*Polq*-double-knockout cells also have increased end resection and elevated RAD51 accumulation[48]. We reasoned that NVB may induce nonfunctional RAD51 foci in HR-deficient tumors with PARPi resistance in vivo. To test this hypothesis, we collected tumor cells from PARPi and/or NVB-treated PDX models and evaluated RAD51 foci by immunohistochemistry (Fig. 4c). As DF83 is an HR-deficient and PARPi-sensitive model, RAD51 foci were not observed. The HR-restored and PARPi-resistant DF59 model, with biallelic mutations in the sequence encoding 53BP1, exhibited a strong increase in RAD51 staining when treated with NVB alone or in combination with olaparib (Fig. 4c,d). Similarly, TOV21G xenograft tumors exhibited increased numbers of RAD51 foci by immunohistochemistry in vivo after NVB treatment, which were further increased by olaparib treatment (Extended Data Fig. 3d–f). Next, we evaluated the effect of NVB on a PARPi-resistant clone (MDA-MB-436-R) of the *BRCA1*-mutated breast cancer cell line MDA-MB-436 (ref. [49]). Similar to the DF59 PDX model, this resistant cell line restored HR by two mechanisms, namely the stabilization of mutant BRCA1 protein and the loss of 53BP1. While highly resistant to olaparib, MDA-MB-436-R cells were sensitive to NVB, similar to the parental cells (Fig. 4e,f). Importantly, NVB induced RAD51 accumulation in MDA-MB-436-R cells but not in the parental cells (Fig. 4g). Because the parental and MDA-MB-436-R cells are both sensitive to NVB, elevated RAD51 levels appear to be nonfunctional for HR, consistent with the increased resection observed in the presence of NVB. In sum, our data suggest that elevated DSB end resection, as well as the subsequent accumulation of ssDNA intermediates and nonfunctional RAD51 loading, are a plausible mechanism of cell killing by NVB in PARPi-resistant HR-deficient tumor cells (Fig. 4h).

NVB overcomes multiple PARPi-resistance mechanisms. To better understand the mechanism by which NVB overcomes PARPi resistance, we generated several PARPi-resistant clones from *BRCA1*$^{-/-}$ RPE1 cells by gradually exposing them to increasing concentrations of PARPi (Fig. 5a). We selected four clones (named R1–R4), all of which acquired resistance to olaparib (Extended Data Fig. 8a–c). Multiple PARPi-resistance mechanisms were identified in these clones, corresponding to published mechanisms[9]. Replication fork stabilization was evident in the R1 and R2 clones (Extended Data Fig. 8d). The R1, R3 and R4 clones had restored RAD51 foci, suggesting restored HR activity in these clones (Extended Data Fig. 8e). The restoration of HR repair in these clones may have resulted in part from downregulation of the Shieldin complex and subsequent downregulation of NHEJ repair. Indeed, the R3 clone had decreased expression of REV7, a component of the Shieldin complex, and the R4 clone had decreased 53BP1 expression (Extended Data Fig. 8f,g). None of the clones re-expressed BRCA1, thereby excluding somatic reversion of BRCA1 as an underlying PARPi-resistance mechanism (Fig. 5b and Extended Data Fig. 8h). Strikingly, all four PARPi-resistant clones remained sensitive to NVB to a similar extent as the parental *BRCA1*$^{-/-}$ RPE1 cells (Fig. 5c,d), suggesting that NVB may overcome multiple mechanisms of acquired resistance to PARPi. To demonstrate that genetic inhibition of POLθ also causes cell death in the PARPi-resistant *BRCA1*$^{-/-}$ clones, we depleted POLθ in R1, R2 and the parental cells and measured cell survival. Upon POLθ depletion, the parental *BRCA1*$^{-/-}$ cells and the PARPi-resistant clones but not WT RPE1 cells showed reduced survival, suggesting that POLθ inhibition was the mechanism for NVB cytotoxicity in those cells (Extended Data Fig. 8i).

We also examined more clinically relevant PARPi-resistant, HR-deficient models, using tumor cells derived from patients. MDA-MB-436-R cells, with stabilized mutant BRCA1 protein and loss of 53BP1, were sensitive to NVB (Fig. 4e,f). In addition, we studied the PARPi-resistant clone UWB1.289-YSR12 (derived from the *BRCA1*-null human ovarian cancer cell line UWB1.289), which acquired resistance to PARPi via stabilization of replication forks[50]. These cells also remained sensitive to NVB, although they were highly resistant to olaparib (Extended Data Fig. 9a,b), again suggesting that acquired resistance to PARPi does not determine cross-resistance to NVB. In sum, these data show that NVB may overcome multiple mechanisms of acquired resistance to PARPi.

POLθ expression is a predictive biomarker for NVB sensitivity. *POLQ* mRNA expression is increased in HR-deficient tumors and in several other cancers associated with poor prognosis[14,51]. We asked whether increased *POLQ* mRNA and POLθ protein expression may serve as a predictive biomarker for NVB sensitivity. As expected, CRISPR-mediated knockout of *BRCA1* in RPE1 cells resulted in higher *POLQ* expression than in the parental cells (Fig. 5e and Extended Data Fig. 9c). Interestingly, all selected PARPi-resistant clones (R1–R4) retained high levels of *POLQ* expression, revealing a direct correlation between *POLQ* expression and NVB sensitivity (Fig. 5e). This correlation was also present in BRCA1-deficient MDA-MB-436 cells. MDA-MB-436-R cells with acquired PARPi resistance exhibited elevated levels of *POLQ* mRNA expression and retained NVB sensitivity, while complementation of the parental cells with WT *BRCA1* cDNA decreased *POLQ* expression and NVB sensitivity (Fig. 5f). The direct correlation of *POLQ* expression and NVB sensitivity was further observed in

Fig. 5 | NVB overcomes multiple PARPi-resistance mechanisms and POLQ expression level is a predictive biomarker for NVB sensitivity. a, A schematic shows how the PARPi-resistant clones R1–R4 were generated. **b**, A western blot of WT and *BRCA1*$^{-/-}$ RPE1 cells and the PARPi-resistant clones, using an anti-BRCA1 antibody (Millipore, OP92). No BRCA1 reversion was observed in the clones. DAPI, 4,6-diamidino-2-phenylindole. **c**,**d**, NVB sensitivity of WT RPE1, *BRCA1*$^{-/-}$ RPE1 and PARPi-resistant *BRCA1*$^{-/-}$ clones (R1–R4). R1 was selected with olaparib, and R2–R4 were selected with niraparib. **c**, R1 and R2 were tested in clonogenic survival assays (12–14 d). **d**, R3 and R4 were tested in the CellTiter-Glo (CTG) cell viability assay (6 d). Data are mean ± s.e.m., $n = 3$ independent cultures. **e**, *POLQ* expression at the mRNA level in WT RPE1, *BRCA1*$^{-/-}$ RPE1 and PARPi-resistant *BRCA1*$^{-/-}$ clones (R1–R4). *POLQ* mRNA levels were measured by qPCR with reverse transcription and normalized to *ACTB* (β-actin). Mean ± s.d. of $n = 4$ independent cultures. R, resistant; S, sensitive. **f**, *POLQ* expression at the mRNA level in parental (P) and PARPi-resistant (R) cells and cells with empty vector or MDA-MB-436 cells complemented with *BRCA1* cDNA (+BR1). Mean ± s.d. of $n = 4$ independent cultures. **g**, *POLQ* expression at the mRNA level in PDX models DF53, DF83 and DF149. Means of four technical replicates for each PDX model are shown. **h**, Olaparib sensitivity of CAPAN1 (*BRCA2* mutated) and CAPAN1-CR cells (with *BRCA2* edited by CRISPR back to WT) in clonogenic survival assays. **i**, NVB sensitivity of CAPAN1 and CAPAN1-CR cells in clonogenic survival assays. Means of $n = 2$ independent experiments are shown in **h**,**i**. Statistical analyses in **h**,**i** were paired *t*-tests, $^*P < 0.05$. **j**, Expression levels of POLQ in CAPAN1 and CAPAN1-CR cells, analyzed by western blotting.

HR-deficient PDX models, in which elevated *POLQ* expression in DF83 and DF59 correlated with high sensitivity to NVB in vivo (Fig. 5g and Fig. 3a–f).

Another known mechanism of PARPi resistance in *BRCA1/2*$^{-/-}$ tumors in the clinic is somatic reversion of *BRCA1/2* genes[4]. We determined whether NVB could overcome PARPi resistance caused

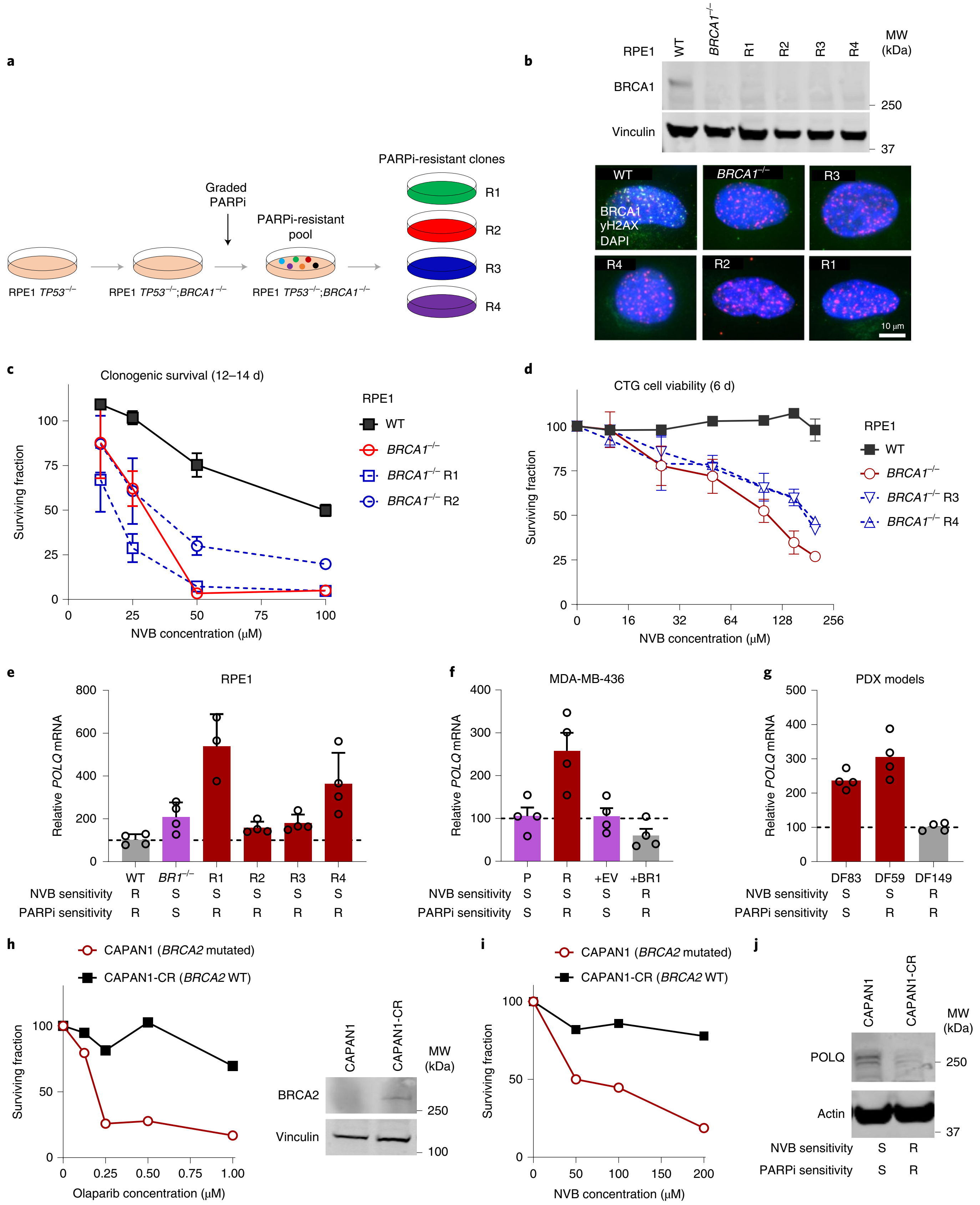

by *BRCA2* reversion. Unlike other PARPi-resistant cells that we analyzed, BRCA2-deficient tumor cells with near-perfect somatic reversion or CRISPR-edited reversion of *BRCA2* (PEO4 and CAPAN1-CR)[10,52] were not only resistant to PARPi but also to NVB, when compared to their HR-deficient parental cell lines (PEO1 and CAPAN1) (Fig. 5h,i and Extended Data Fig. 9d,e). These data suggest that NVB can overcome some but not all mechanisms of PARPi resistance. Importantly, low levels of *POLQ* expression were a predictive biomarker for NVB resistance. For PARPi-resistant cell lines with *BRCA2* reversion mutations (PEO4 and CAPAN1-CR), resistance to NVB correlated with low levels of POLθ protein expression by western blot (Fig. 5j and Extended Data Fig. 9f). The resistance of the DF149 PDX model in vivo correlated with its low levels of *POLQ* expression (Fig. 5g). Also, the loss of POLθ in RPE1 cells correlated with resistance to NVB (Fig. 2e). In sum, in all cases we examined, POLθ expression levels correlated with cellular sensitivity to NVB, suggesting that POLθ expression in a tumor biopsy could provide a convenient predictive biomarker for patient enrollment in future clinical trials with NVB or other POLθ inhibitors.

Discussion

In summary, NVB is a specific and potent POLθ inhibitor that phenocopies POLθ depletion and is synthetic lethal in HR-deficient tumors. In the clinic, many tumors with acquired PARPi resistance are likely to remain sensitive to NVB, depending on their mechanism of resistance. Tumors that acquire PARPi resistance by downregulating NHEJ and partially restoring HR repair remain sensitive to NVB. For these tumors, the persistent high level of POLθ expression is a predictive biomarker for their NVB responsiveness, and NVB-induced RAD51 accumulation provides a convenient pharmacodynamic biomarker for clinical trials.

Our work provides mechanistic insights into the cause of synthetic lethality induced by NVB. BRCA1/2-deficient, HR-defective tumor cells are hyperdependent on POLθ, which is recruited for MMEJ by PARP at DSBs and by repair protein XRCC1 along with MRE11 at replication forks[14,53]. Accordingly, NVB kills these HR-deficient cells by blocking the tumor-critical MMEJ activity of POLθ. On the other hand, BRCA1/2-deficient tumor cells that have acquired PARPi resistance, resulting from the downregulation of 53BP1 or other Shieldin components, appear to require POLθ activity for limiting end resection. Accordingly, NVB kills these tumor cells by enhancing end resection, leading to toxic levels of ssDNA intermediates and nonfunctional RAD51 loading.

Finally, our findings may translate to a potential new therapy for treating HR-deficient tumors in addition to PARP inhibition. Importantly, NVB is an oral and well-tolerated drug, and it has previously been investigated in phase 1 cancer trials[32–35]. Some partial responses were documented, even though the enrolled patients were not preselected for HR-deficient cancer[32]. Other previous clinical studies showed that the serum concentration at which NVB specifically kills HR-deficient cells (that is, 100 µM) is readily achievable without causing adverse side effects in humans[33–35]. In addition, the half-life of NVB in humans (6.0 h) is substantially longer than its half-life in mice (82 min)[32], suggesting that NVB may be even more efficacious in humans than in our mouse models. In summary, results in this study provide a strong rationale for future clinical studies of NVB alone or in combination with PARPi to prevent or overcome PARPi resistance.

Methods

Compounds, inhibitors and antibodies. Chemical compounds, including PARPi olaparib (S1060) and rucaparib (S1098), NVB (S2492), etoposide (S1225) and PU-H71 (S8039) were purchased from Selleckchem. Chemicals were dissolved in DMSO and kept in small aliquots at −80 °C. The key sources of antibodies are anti-POLθ (Sigma, SAB1402530), anti-γH2AX (Millipore, 05-636), anti-RAD51 (Santa Cruz Biotechnology, SCB, sc-8349), anti-CDK6 (SCB, sc-7961), anti-AKT1 (SCB, sc-5298), anti-HSP70 (SCB, sc-24), anti-HSP90 (SCB, sc-13119) and anti-FANCF (Everest Biotech, EB06112).

Protein purification. DNA encoding a POLθ fragment (ΔPol) containing the ATPase domain with a RAD51-binding site (amino acids 1–987) was cloned into pFastBac-C-Flag and purified from baculovirus-infected SF9 insect cells. POLθ-expressing cells were lysed in lysis buffer (500 mM NaCl, 0.01% NP-40, 0.2 mM EDTA, 20% glycerol, 1 mM dithiothreitol, 0.2 mM phenylmethylsulfonyl fluoride, 20 mM Tris (pH 7.6)) supplemented with Halt Protease Inhibitor Cocktail (Thermo Fisher) and Calpain I Inhibitor (Roche). Cell lysates were incubated with M2 anti-FLAG beads (Sigma) for 3 h at 4 °C on a spinning wheel. Beads were washed three times with lysis buffer, and protein was then eluted in lysis buffer supplemented with 0.2 mg ml^{-1} FLAG peptide (Sigma). The protein was then concentrated in lysis buffer using 10-kDa centrifugal filters (Amicon). SMARCAL1, CHD1, BLM, RAD51 and TRIP13 were purified in house using a similar protocol. The ATPase domain of BLM and the MRE11 catalytic domain were purified by affinity followed by gel-filtration chromatography. Purified HSP90AA1 protein was purchased from Abcam (ab78425).

High-throughput small-molecule screen. The ATPase activity-based high-throughput small-molecule screen was performed at the ICCB-Longwood Screening Facility at Harvard Medical School. On the day of screening, a Combi machine was used to dispense 10-µl aliquots of a master mix containing 600 nM of 30-mer ssDNA substrate and 10 nM POLθ protein (ΔPol) into each well of a 384-well plate (Corning, 3820). Small molecules were added to wells in the 384-well plates with a Seiko Pin transfer robot. Plates were covered with aluminum seals and centrifuged at 1,000 r.p.m. and sat for 1 h to allow small molecules to bind protein. Ultra-pure ATP (3 µl, 433.33 µM) was added to every well except for no-substrate control wells. Plates were stored overnight (16 h) in a humidified plastic chamber. The next day, 6.5 µl ADP-Glo reagent (Promega) was added to every well using the Combi machine. After a 1-h incubation, 13 µl Kinase Detection Reagent (Promega) was added to every well, and plates were incubated for another hour. Data were collected using the EnVision plate reader by measuring luminescent signals. More information about the screen is available in Supplementary Table 1.

Statistical analysis of the high-throughput screen. The inhibition strength of screened compounds was evaluated using a Z-score analysis. As most compounds did not affect POLθ ATPase activity, data for all compounds was used to calculate plate mean (μ) and standard deviation (σ) values. Every compound was then assigned *a Z* score using the equation $Z = (x - \mu) \times \sigma^{-1}$. Percent inhibition of compounds was determined by normalizing to values from the DMSO control. Values from wells with DMSO were averaged to find the average signal without inhibitor, and a different average of values from DMSO controls was calculated for each plate. Percent activity was calculated using the following formula: percent activity = [(signal with compound) × (average signal with DMSO)$^{-1}$] × 100%.

ATPase activity assay. The ATPase activity of POLθ was measured using the ADP-Glo kinase assay (Promega). Reactions were carried out in 50 µl reaction buffer (40 mM Tris-HCl buffer (pH 7.6), 20 mM $MgCl_2$, 0.1 mg ml^{-1} BSA and 1 mM dithiothreitol) in black 96-well plates. Final concentrations were 600 nM of 30-mer ssDNA, 50 nM of purified POLθ ΔPol protein and 100 µM of ATP, with DMSO or NVB. The sequence of the 30-mer ssDNA used in the assay was 5′-CCAGTGAATTGTTGCTCGGTACCTGCTAAC-3′. The order for adding the components was 10 µl 1× reaction buffer, 10 µl 10× ssDNA, 10 µl 10× POLθ, 10 µl 10× NVB or DMSO (incubate at room temperature for 15 min) and finally 10 µl 10× ATP, and all components were prepared in 1× reaction buffer. Control wells with DMSO represented 0% inhibition, while wells with no enzyme represented 100% inhibition. Plates were covered with an aluminum seal and incubated at room temperature overnight (16 h). The following day, 50 µl ADP-Glo reagent (Promega kit) was added to each reaction well and incubated at room temperature for 1 h. Next, 100 µl kinase detection reagent (Promega kit) was added to the wells, and plates were incubated for another hour. Finally, ATP hydrolysis was quantified by luminescence measured on a plate reader. Measurements of other ATPases were carried out using the same conditions and protocol. In some cases, as indicated, a ^{32}P-based ATPase activity assay was also performed as previously described[54].

Thermal stability assays. The POLθ helicase domain was expressed using the POLQ-A construct (Addgene, 74645) in HF insect cells and purified as described previously[30]. Thermal stability of the POLθ helicase domain in the presence of NVB was measured using Prometheus with NanoDSF (NanoTemper). Given that the intrinsic fluorescence emission from the protein coincides with the chromophore core in NVB, we monitored scattering to measure protein stability with temperature. The POLθ helicase domain (0.5 mg ml^{-1} in 25 mM HEPES (pH 8) and 200 mM NaCl) was incubated with the indicated concentration of NVB for 30 min before the sample was loaded into capillaries for scattering measurements with increasing temperature at 1 °C per minute, starting from 25 °C until 90 °C. Shifts in the maximum peak of scattering were estimated from the first derivative of the scattering data. All data points were an average from three replicates and were plotted in GraphPad Prism 8.

Preparation of NVB–Sepharose 6B beads. NVB–Sepharose 6B beads were prepared similarly as previously described[55]. Epoxy-activated Sepharose 6B (0.5 g)

(Sigma-Aldrich, E6754) was washed thoroughly and swollen in 50 ml distilled water for 1 h at room temperature. The resin was washed once with coupling buffer (0.3 M sodium carbonate (pH 9.5)). The washed resin was mixed with 500 mg NVB in 50 ml coupling buffer and incubated at 37 °C with rotation overnight. The next day, the resin was washed with coupling buffer three times to remove excess NVB. The remaining epoxy-active groups were blocked with 1 M ethanolamine (in coupling buffer) for 6 h at 37 °C with gentle rotation. Beads were sequentially washed with coupling buffer, 0.5 M NaCl in coupling buffer, distilled water, 0.5 M NaCl in 0.1 M sodium acetate (pH 4) and twice with distilled water. Beads were resuspended and stored in 25 mM HEPES (pH 7.6), 200 mM KCl, 10% ethylene glycol and 1 mM EDTA.

GFP reporter-based DNA repair assays. U2OS cells containing the DR-GFP (for HR) and EJ2 (for MMEJ) repair substrates were gifts from J. Stark at the Beckman Research Institute of the City of Hope. To measure repair efficiency, 1×10^5 cells were plated in each well of a 12-well plate. Indicated compounds or DMSO were added to the medium for 24 h, and cells were infected with adenoviruses expressing the I-SceI enzyme. Two days after infection, cells were trypsinized, and GFP-positive cells were quantified by flow cytometry (Beckman).

RAD51- and γH2AX-focus formation assay. Cells were pretreated with DMSO or NVB for 24 h before receiving 5 Gy irradiation. After irradiation (4–8 h), cells were extracted and fixed with 1% PFA, 0.5% methanol and 0.5% Triton X-100 in PBS for 20 min at room temperature on a shaker. Fixed cells were washed with PBS twice and blocked with BTG buffer (1 mg ml^{-1} BSA, 0.5% Triton X-100, 3% goat serum, 1 mM EDTA) for 1 h. Cells were then incubated with a rabbit anti-RAD51 antibody (Santa Cruz Technology, sc-8349 or Cell Signaling Technology, 8875) and a mouse anti-γH2AX antibody (Millipore, 05-636) in BTG buffer. After washing with PBS three time, cells were incubated with Alexa 488 (Life Technologies, A11034)- or Alexa 594 (Life Technologies, A11005)-conjugated secondary antibodies in BTG buffer for 1 h. Dishes were washed with BTG buffer once and with PBS twice and mounted with mounting solution with DAPI for immunofluorescence microscopy. Images of random fields were taken under a ×63 oil lens. Foci were visualized and quantified using ImageJ software. Images were prepared in Zen software version 3.1 (Zeiss, blue edition).

CellTiter-Glo cell viability assay. The CellTiter-Glo luminescent cell viability assay kit (Promega, G7573) was used to measure cell viability after drug treatment. The CellTiter-Glo kit determines the number of viable cells in culture based on quantitation of the ATP present, an indicator of metabolically active cells. In total, 500–1,000 cells per well were seeded in a 96-well plate in a volume of 100 µl medium. Twenty-four hours later, cells were treated with the indicated drugs by adding 100 µl medium containing 2× concentrated drug of the desired final concentration. Cells were cultured in drug-containing medium for 6 d, when cell viability was determined by measuring the luminescent signal, following the manufacturer's instructions. The surviving fraction of drug-treated cells was normalized to values from the DMSO-treated control. Survival, IC$_{50}$ and statistics were determined by using GraphPad Prism software.

Clonogenic survival assay. Cells were seeded, at two different concentrations, into each well of a 6-well plate (100 and 200 cells for WT RPE1; 500 and 1,000 cells for HR-deficient cells). The next day, cells were treated with the indicated doses of inhibitors. For combination studies, cells were treated first with NVB or DMSO for 24 h, washed and then incubated in fresh medium containing NVB or DMSO with increasing concentrations of PARPi. Cells were allowed to grow in drug-containing medium for 12–14 d. Cells were fixed and stained with 0.2% crystal violet in methanol for 30 min (Crystal Violet solution, Sigma, HT90132) and rinsed with distilled water three times. Stained dishes were air dried, and the number of colonies (>50 cells) in each well was counted. Surviving fractions were plotted for each drug concentration by normalizing values to those of untreated cells.

Gene knockouts and cell line generation. *BRCA1*, *BRCA2* and *POLQ* knockouts were generated in RPE1 cells in which *TP53* was first knocked out (RPE1 *TP53*$^{-/-}$). *BRCA1* knockouts were previously generated in RPE1 *TP53*$^{-/-}$ cells (named here RPE.1a) in A.D.D.'s laboratory (Dana-Farber Cancer Institute, DFCI)[56]. *BRCA2* and *POLQ* knockouts were generated in R.C.'s laboratory (Institut Curie) using another clone of RPE1 *TP53*$^{-/-}$ cells (named here RPE.1b). Accordingly, we named the following knockouts: RPE1a *BRCA1*$^{-/-}$ and RPE1b *POLQ*$^{-/-}$, RPE1b *BRCA2*$^{-/-}$. Knockouts were generated by cotransfection of Cas9 (pSpCas9(BB)-2A-GFP, Addgene, 48138) (PX458) and sgRNA vectors (gRNA cloning vector plasmid, Addgene, 41824) with the Lipofectamine LTX with Plus Reagent (Thermo Fisher). After subcloning into a 96-well plate, single colonies were screened by PCR. Briefly, DNA was extracted by adding 30 µl of a 50 mM NaOH solution per well, after which the plate was put at 95 °C for 10 min. Next, 2.5 µl 1 M Tris-HCl, pH 7.5, was added per well, and 2 µl of the extracted DNA was used to perform a screening PCR (Terra PCR Direct Polymerase, Takara Clontech). Clones were selected for the presence of the deletion PCR band and the absence of the 5′ and 3′ junction PCR band. RPE1b cells were obtained using the TP53 sgRNA sequence: GGCAGCTACGGTTTCCGTC. RPE1b *BRCA2*$^{-/-}$ cells and RPE1b *POLQ*$^{-/-}$ cells were obtained using two sgRNA vectors targeting introns flanking exon 2 of the *BRCA2* gene: BRCA2-2, GGTAAAACTCAGAAGCGC; BRCA2-3, GCAACACTGTGACGTACT or the *POLQ* gene: POLQ-2, GGAAGGCTTTTAGGTCAGTA; POLQ-3, GGCAACGGGGGCAGCTCCGC. PCR primer sequences used for genotyping the *BRCA2* knockout were the following: deletion PCR (seqBRCA2-For, GCTGTATTCCGAAGACATGCTGATGG; seqBRCA2-Rev, TTGTTCCTACTGCTAGTCAAGGG), 5′ junction PCR (seqBRCA2-For and exon2-Rev, TACCTACGATATTCCTCCAATGCTT) and 3′ junction PCR (seqBRCA2-Rev and exon2-For, AAGCATTGGAGGAATATCGTAGGTA). For genotyping the *POLQ* knockout, we used the following primers: deletion PCR (seqPOLQ-For, GAAGAGCTACTTCCCTGATCTACC; seqPOLQ-Rev, CCCAACCAATCTCATTACGAATCC), 5′ junction PCR (seqPOLQ-For and exon2-Rev, GAGCCTGATTCTGAACGCCGCCG) and 3′ junction PCR (seqBRCA2-Rev and exon2-For, CGGCGGCGTTCAGAATCAGGCTC).

POLQ-knockout cells were generated in U2OS cells as well. Cas9 was introduced into U2OS cells by lentiviral infection using the lentiCas9-Blast plasmid (Addgene, 52962), and stable Cas9-expressing U2OS cells (U2OS-Cas9) were obtained after blasticidin selection. sgRNA oligonucleotides designed to target the genomic sequence GATTCGTTCTCGGGAAGCGG of *POLQ* (exon 1) were annealed and inserted into the LentiGuide-Puro plasmid (a gift from F. Zhang at the Broad Institute, Addgene# 52963). After lentiviral infection, U2OS-Cas9 cells were selected with puromycin for 3 d, and the surviving cells were trypsinized and seeded sparsely to form single-cell colonies. Colonies were picked and expanded, and genomic DNA from individual clones was isolated with the QIAamp DNA Mini kit (Qiagen). PCR was performed to amplify the gRNA-targeted region (216 bp) using the following primers: forward, GGAGGACGCTGGGACTGTGGC; reverse, CTGCAGCTGCGGCCTTCAGGC. PCR products were cleaned with the PCR purification kit (Qiagen) and submitted for next-generation sequencing (amplicon sequencing performed by Genewiz). Sequencing reads were mapped to the human genome at the *POLQ* locus, and results were visualized with the Integrative Genomics Viewer (Broad Institute). Clones with homologous deletion of the *POLQ* gene were confirmed by western blot analysis. Images of western blots were collected using Odyssey Infrared Imagers (LI-COR) and analyzed using Image Studio Lite.

Cloning, PiggyBac constructions and cell line generation. WT full-length *POLQ* cDNA was assembled by PCR with a FLAG-P2A-BLAST cassette and subsequently cloned by Gibson assembly (New England Biolabs, E2611L) in the PiggyBac PBCAG-eGFP vector (Addgene, 40973) using BsrGI and SbfI sites to obtain the PiggyBac-eGFP-POLQ-FLAG-P2A-BLAST vector (referred to here as GFP–Polθ WT). Point mutations were introduced using PCR mutagenesis and Gibson assembly in active sites as follows: helicase (K121A, DE-216/7-AA), polymerase (DE-2540/1-AA), helicase and polymerase (K121A, DE-216/7-AA, DE-2540/1-AA). RPE1b *POLQ*$^{-/-}$ cells were complemented with GFP–Polθ WT and mutant constructs. Cells were plated in a 6-well plate, transfected the day after with 1 µg PiggyBac vector and 0.5 µg PiggyBac transposase (System Biosciences, PB210PA-1) using Lipofectamine LTX with Plus Reagent (Thermo Fisher) and selected with blasticidin (21 µg ml^{-1}) for 10 d. Vector expression was confirmed by western blot.

Laser micro-irradiation. RPE1b *POLQ*$^{-/-}$ cells expressing eGFP–POLθ constructs were plated in a 35-mm µ-Dish with a glass bottom (Ibidi, 81158). The day after, DMSO (0.1%) or NVB (100 µM) was added to the cells for 16 h. The medium was replaced with fresh medium (with DMSO or NVB) 2 h before irradiation. Micro-irradiation was performed with a two-photon laser (800 nm, 20% power) on an inverted laser scanning confocal microscope equipped with spectral detection and a multi-photon laser (LSM880NLO/Mai Tai Laser, Zeiss, Spectra-Physics) with an Airyscan module. Images were analyzed using the 'Plot Z-Axis Profile' macro on Fiji (version 2.1.0/1.53c). RPE1b *POLQ*$^{-/-}$ cells expressing the PBCAG-eGFP vector were used as a control.

Mouse xenograft and PDX studies. All animal experiments were conducted in accordance with Institutional Animal Care and Use Committee-approved protocols at the Beth Israel Deaconess Medical Center and the DFCI. For PDX studies, tumor ascites were collected from patients with suspected or established ovarian cancer at the Brigham and Women's Hospital or the DFCI under IRB-approved protocols conducted in accordance with the Declaration of Helsinki and the Belmont Report. Written informed consent was obtained from patients when required.

TOV21G xenograft study. Female NU(NCr)-*Foxn1*^{nu} athymic nude mice were purchased from Charles River for TOV21G xenograft experiments. In total, 5×10^5 TOV21G cells with empty vector or TOV21G cells complemented with FANCF in PBS were mixed with an equal volume of Matrigel (Corning) and injected subcutaneously into the flanks of mice. Mice were then randomly assigned to four treatment groups: (1) TOV21G cells with empty vector, PBS, (2) TOV21G cells with empty vector, NVB, (3) TOV21G cells complemented with FANCF, PBS and (4) TOV21G cells complemented with FANCF, NVB. Four days after tumor cell implantation, mice were treated with NVB (100 mg per kg) or PBS twice a day via i.p. injection for 4 weeks. Tumors were measured every 2–3 d using an electronic caliper, and tumor volumes were calculated by using the formula $L \times W \times W \div 2$, where L is length and W is width.

Genetically engineered mouse models. Pieces from breast tumors generated in K14-Cre-*Brca1*$^{f/f}$;*Trp53*$^{f/f}$ female mice were transplanted into the mammary fat pad of FVB/129P2 recipient females that were at least 6 weeks old. FVB/129P2 recipients were generated by breeding FVB females (Jackson Laboratory) and 129P2 males (Envigo) and using the first-generation litters for experimentation. When tumors reached approximately 150 mm^3 in volume, mice were randomized into treatment groups (vehicle and NVB). Treatment continued until tumors reached 20 mm in any direction, at which point mice were euthanized. NVB was prepared fresh from powder in PBS each time before i.p. injection and administered at 100 mg per kg twice a day for 35 d. Tumors were measured every 3–4 d using an electronic caliper, and tumor volumes were calculated by using the formula $L \times W \times W \div 2$.

Patient-derived xenograft studies. PDX models were established, luciferized and propagated at the DFCI and were described previously[57]. Approximately $2–10 \times 10^6$ luciferized PDX cells derived from mouse ascites were injected i.p. into 8-week-old female NSG mice. Tumor burden was measured by BLI using a Xenogen IVIS 200 system (Xenogen). Mice were grouped according to BLI signals from tumors so that each group would have similar initial average BLI values. NVB was diluted in saline and administered via i.p. injection at 75 mg per kg twice daily for 4 weeks. Olaparib (ChemExpress) was formulated in PBS containing 10% DMSO and 10% (wt/vol) 2-hydroxypropyl-β-cyclodextrin (Sigma-Aldrich) and administered orally at 50 mg per kg daily for 4 weeks.

Quantitative RT–PCR. Total RNA was extracted using the RNeasy Mini kit (Qiagen), and cDNA was generated using the SuperScript III First-Strand Synthesis kit (Thermo Fisher). The PowerUp SYBR Green Master Mix (Thermo Fisher) reagent was used to run qPCR on a QuantStudio 7 Flex Real-Time PCR System (Applied Biosystems). Two set of *POLQ* primers were used, which gave the same *POLQ* mRNA measurements: *POLQ* primer set 1 (forward, 5′-TATCTGCTGG AACTTTTGCTGA-3′; reverse, 5′-CTCACACCATTTCTTTGATGGA-3′); *POLQ* primer set 2 (forward, 5′-CTACAAGTGAAGGGAGATGAGG-3′; reverse, 5′-TCAGAGGGTTTCACCAATCC-3′). Internal control primers were *ACTB* (forward, 5′-CACCATTGGCAATGAGCGGTTC-3′; reverse, 5′-AGGTCTT TGCGGATGTCCACGT-3′) or *GAPDH* (forward, 5′-GTCTCCTCTGACT TCAACAGCG-3′; reverse, 5′-ACCACCCTGTTGCTGTAGCCAA-3′).

Immunohistochemistry. NSG mice bearing DF59 and DF83 tumors were dosed as described in the efficacy study, with 75 mg per kg NVB twice a day and with 50 mg per kg olaparib daily. Four hours after the last dose (52 h after the first dose), tumor cells were isolated from the peritoneum of the mice, cleaned, washed with PBS and fixed in 10% normal buffered formalin for 10 min at room temperature. Next, tumor cells were washed with PBS three times and embedded in HistoGel (Richard-Allan Scientific). HistoGel cores were processed using standard histology methods and embedded in paraffin. RAD51 staining was performed on paraffin sections (4 µm) using a previously standardized protocol (https://doi.org/10.1158/1538-7445.AM2017-2796). Images of stained slides were acquired on an Olympus BX41 microscope equipped with a digital camera at ×40 magnification. The percentage of RAD51-foci-positive cell fields was estimated.

Molecular docking. We used the AMP-PNP-Mg^{2+}-bound POLθ-HD (PDB 5AGA) structure for our docking studies, as it has the best resolution (2.9 Å) among the reported structures in the PDB[30]. For docking studies, the protein structure was prepared using the Protein Preparation Wizard from the Schrödinger suite. AMP-PNP-Mg^{2+} was stripped from the structure as well. Using the minimized structure, a 25-Å grid created around the Asn451 residue, given its close proximity to the ADP and AMP-PNP binding site in the helicase domain, was used to search for a potential binding site for NVB. The LigPrep Wizard from the Schrödinger suite was used to prepare NVB ligand in different protonated states for docking. All minimizations in the Protein Prep and LigPrep wizards were performed with the OPLS3 force field[58]. The Glide Extra Precision docking module of the Schrödinger workflow was used to produce NVB and POLθ-HD complex structure with the best scoring poses[59]. For all the generated poses, binding free energy MM-GBSA calculations were performed using the Prime module, and the best model was selected based on the resulting protein–ligand complex with the lowest MM-GBSA binding free energy value[60].

Statistics and reproducibility. No statistical methods were used to predetermine sample sizes. Experiments were not randomized, except for mouse studies, in which mice were randomized based on their initial tumor sizes to achieve an approximately equal mean. No data were excluded from the analyses. The person who performed mouse xenograft studies was blinded to the identities of the tumor cells. The person who performed PDX studies was blinded to the genotypes of the tumors being studied. For other studies, no specific blinding method was used. Statistical analyses performed are specified in the figure legends. Statistical analyses were performed in Prism version 8 (GraphPad). Error bars represent ±s.d. or ±s.e.m. as described in figure legends, and P values are indicated by $^{*}P < 0.05$, $^{**}P < 0.01$, $^{***}P < 0.001$ and $^{****}P < 0.0001$, unless values are given.

Reporting Summary. Further information is available in the Nature Research Reporting Summary linked to this article.

Data availability

All related data are presented in this manuscript. Complete results of the small-molecule screen and lists of top hits are provided in Supplementary Tables 1–4. Source data are provided with this paper.

Received: 30 September 2020; Accepted: 24 March 2021;

References

1. Lord, C. J. & Ashworth, A. PARP inhibitors: synthetic lethality in the clinic. *Science* **355**, 1152–1158 (2017).
2. Farmer, H. et al. Targeting the DNA repair defect in *BRCA* mutant cells as a therapeutic strategy. *Nature* **434**, 917–921 (2005).
3. Bryant, H. E. et al. Specific killing of BRCA2-deficient tumours with inhibitors of poly(ADP-ribose) polymerase. *Nature* **434**, 913–917 (2005).
4. Konstantinopoulos, P. A., Ceccaldi, R., Shapiro, G. I. & D'Andrea, A. D. Homologous recombination deficiency: exploiting the fundamental vulnerability of ovarian cancer. *Cancer Discov.* **5**, 1137–1154 (2015).
5. Ledermann, J. et al. Olaparib maintenance therapy in platinum-sensitive relapsed ovarian cancer. *N. Engl. J. Med.* **366**, 1382–1392 (2012).
6. Coleman, R. L. et al. Rucaparib maintenance treatment for recurrent ovarian carcinoma after response to platinum therapy (ARIEL3): a randomised, double-blind, placebo-controlled, phase 3 trial. *Lancet* **390**, 1949–1961 (2017).
7. Mirza, M. R. et al. Niraparib maintenance therapy in platinum-sensitive, recurrent ovarian cancer. *N. Engl. J. Med.* **375**, 2154–2164 (2016).
8. Litton, J. K. et al. Talazoparib in patients with advanced breast cancer and a germline *BRCA* mutation. *N. Engl. J. Med.* **379**, 753–763 (2018).
9. Lord, C. J. & Ashworth, A. Mechanisms of resistance to therapies targeting *BRCA*-mutant cancers. *Nat. Med.* **19**, 1381–1388 (2013).
10. Sakai, W. et al. Secondary mutations as a mechanism of cisplatin resistance in *BRCA2*-mutated cancers. *Nature* **451**, 1116–1120 (2008).
11. Ray Chaudhuri, A. et al. Replication fork stability confers chemoresistance in BRCA-deficient cells. *Nature* **535**, 382–387 (2016).
12. Noordermeer, S. M. et al. The Shieldin complex mediates 53BP1-dependent DNA repair. *Nature* **560**, 117–121 (2018).
13. Ghezraoui, H. et al. 53BP1 cooperation with the REV7–Shieldin complex underpins DNA structure-specific NHEJ. *Nature* **560**, 122–127 (2018).
14. Ceccaldi, R. et al. Homologous-recombination-deficient tumours are dependent on Polθ-mediated repair. *Nature* **518**, 258–262 (2015).
15. Ceccaldi, R., Rondinelli, B. & D'Andrea, A. D. Repair pathway choices and consequences at the double-strand break. *Trends Cell Biol.* **26**, 52–64 (2016).
16. Mateos-Gomez, P. A. et al. Mammalian polymerase θ promotes alternative NHEJ and suppresses recombination. *Nature* **518**, 254–257 (2015).
17. Wood, R. D. & Doublie, S. DNA polymerase θ (POLQ), double-strand break repair, and cancer. *DNA Repair* **44**, 22–32 (2016).
18. Seki, M. et al. High-efficiency bypass of DNA damage by human DNA polymerase Q. *EMBO J.* **23**, 4484–4494 (2004).
19. Yoon, J. H. et al. Error-prone replication through UV lesions by DNA polymerase θ protects against skin cancers. *Cell* **176**, 1295–1309 (2019).
20. Chan, S. H., Yu, A. M. & McVey, M. Dual roles for DNA polymerase θ in alternative end-joining repair of double-strand breaks in *Drosophila*. *PLoS Genet.* **6**, e1001005 (2010).
21. Goff, J. P. et al. Lack of DNA polymerase θ (POLQ) radiosensitizes bone marrow stromal cells in vitro and increases reticulocyte micronuclei after total-body irradiation. *Radiat. Res.* **172**, 165–174 (2009).
22. Audebert, M., Salles, B. & Calsou, P. Involvement of poly(ADP-ribose) polymerase-1 and XRCC1/DNA ligase III in an alternative route for DNA double-strand breaks rejoining. *J. Biol. Chem.* **279**, 55117–55126 (2004).
23. Seki, M., Marini, F. & Wood, R. D. POLQ (Pol θ), a DNA polymerase and DNA-dependent ATPase in human cells. *Nucleic Acids Res.* **31**, 6117–6126 (2003).
24. Ozdemir, A. Y., Rusanov, T., Kent, T., Siddique, L. A. & Pomerantz, R. T. Polymerase θ-helicase efficiently unwinds DNA and RNA–DNA hybrids. *J. Biol. Chem.* **293**, 5259–5269 (2018).
25. Mateos-Gomez, P. A. et al. The helicase domain of Polθ counteracts RPA to promote alt-NHEJ. *Nat. Struct. Mol. Biol.* **24**, 1116–1123 (2017).
26. Zahn, K. E., Jensen, R. B., Wood, R. D. & Doublie, S. Human DNA polymerase θ harbors DNA end-trimming activity critical for DNA repair. *Mol. Cell* **81**, 1534–1547 (2021).
27. Beagan, K. et al. *Drosophila* DNA polymerase θ utilizes both helicase-like and polymerase domains during microhomology-mediated end joining and interstrand crosslink repair. *PLoS Genet.* **13**, e1006813 (2017).
28. Higgins, G. S. & Boulton, S. J. Beyond PARP–POLθ as an anticancer target. *Science* **359**, 1217–1218 (2018).

29. Yusufzai, T. & Kadonaga, J. T. HARP is an ATP-driven annealing helicase. *Science* **322**, 748–750 (2008).
30. Newman, J. A., Cooper, C. D. O., Aitkenhead, H. & Gileadi, O. Structure of the helicase domain of DNA polymerase θ reveals a possible role in the microhomology-mediated end-joining pathway. *Structure* **23**, 2319–2330 (2015).
31. Higgins, G. S. et al. A small interfering RNA screen of genes involved in DNA repair identifies tumor-specific radiosensitization by POLQ knockdown. *Cancer Res.* **70**, 2984–2993 (2010).
32. Eder, J. P., Wheeler, C. A., Teicher, B. A. & Schnipper, L. E. A phase I clinical trial of novobiocin, a modulator of alkylating agent cytotoxicity. *Cancer Res.* **51**, 510–513 (1991).
33. Drusano, G. L. et al. Steady-state serum pharmacokinetics of novobiocin and rifampin alone and in combination. *Antimicrob. Agents Chemother.* **30**, 42–45 (1986).
34. Kennedy, M. J. et al. Phase I and pharmacologic study of the alkylating agent modulator novobiocin in combination with high-dose chemotherapy for the treatment of metastatic breast cancer. *J. Clin. Oncol.* **13**, 1136–1143 (1995).
35. Murren, J. R. et al. Phase I and pharmacokinetic study of novobiocin in combination with VP-16 in patients with refractory malignancies. *Cancer J.* **6**, 256–265 (2000).
36. Liu, X. et al. Somatic loss of BRCA1 and p53 in mice induces mammary tumors with features of human *BRCA1*-mutated basal-like breast cancer. *Proc. Natl Acad. Sci. USA* **104**, 12111–12116 (2007).
37. Pantelidou, C. et al. PARP inhibitor efficacy depends on CD8$^+$ T-cell recruitment via intratumoral STING pathway activation in BRCA-deficient models of triple-negative breast cancer. *Cancer Discov.* **9**, 722–737 (2019).
38. Turner, N., Tutt, A. & Ashworth, A. Hallmarks of 'BRCAness' in sporadic cancers. *Nat. Rev. Cancer* **4**, 814–819 (2004).
39. Taniguchi, T. et al. Disruption of the Fanconi anemia–BRCA pathway in cisplatin-sensitive ovarian tumors. *Nat. Med.* **9**, 568–574 (2003).
40. Sugino, A., Higgins, N. P., Brown, P. O., Peebles, C. L. & Cozzarelli, N. R. Energy coupling in DNA gyrase and the mechanism of action of novobiocin. *Proc. Natl Acad. Sci. USA* **75**, 4838–4842 (1978).
41. Marcu, M. G., Chadli, A., Bouhouche, I., Catelli, M. & Neckers, L. M. The heat shock protein 90 antagonist novobiocin interacts with a previously unrecognized ATP-binding domain in the carboxyl terminus of the chaperone. *J. Biol. Chem.* **275**, 37181–37186 (2000).
42. Hsieh, T. & Brutlag, D. ATP-dependent DNA topoisomerase from *D. melanogaster* reversibly catenates duplex DNA rings. *Cell* **21**, 115–125 (1980).
43. Pocklington, M. J., Jenkins, J. R. & Orr, E. The effect of novobiocin on yeast topoisomerase type II. *Mol. Gen. Genet.* **220**, 256–260 (1990).
44. Drean, A., Lord, C. J. & Ashworth, A. PARP inhibitor combination therapy. *Crit. Rev. Oncol. Hematol.* **108**, 73–85 (2016).
45. Mirza, M. R., Pignata, S. & Ledermann, J. A. Latest clinical evidence and further development of PARP inhibitors in ovarian cancer. *Ann. Oncol.* **29**, 1366–1376 (2018).
46. Parmar, K. et al. The CHK1 inhibitor prexasertib exhibits monotherapy activity in high-grade serous ovarian cancer models and sensitizes to PARP inhibition. *Clin. Cancer Res.* **25**, 6127–6140 (2019).
47. Zhou, Y., Caron, P., Legube, G. & Paull, T. T. Quantitation of DNA double-strand break resection intermediates in human cells. *Nucleic Acids Res.* **42**, e19 (2013).
48. Feng, W. et al. Genetic determinants of cellular addiction to DNA polymerase θ. *Nat. Commun.* **10**, 4286 (2019).
49. Johnson, N. et al. Stabilization of mutant BRCA1 protein confers PARP inhibitor and platinum resistance. *Proc. Natl Acad. Sci. USA* **110**, 17041–17046 (2013).
50. Yazinski, S. A. et al. ATR inhibition disrupts rewired homologous recombination and fork protection pathways in PARP inhibitor-resistant BRCA-deficient cancer cells. *Genes Dev.* **31**, 318–332 (2017).
51. Lemee, F. et al. DNA polymerase θ up-regulation is associated with poor survival in breast cancer, perturbs DNA replication, and promotes genetic instability. *Proc. Natl Acad. Sci. USA* **107**, 13390–13395 (2010).
52. Barber, L. J. et al. Comprehensive genomic analysis of a BRCA2 deficient human pancreatic cancer. *PLoS ONE* **6**, e21639 (2011).
53. Eckelmann, B. J. et al. XRCC1 promotes replication restart, nascent fork degradation and mutagenic DNA repair in BRCA2-deficient cells. *NAR Cancer* **2**, zcaa013 (2020).
54. Zhou, J. et al. Human CHD1 is required for early DNA-damage signaling and is uniquely regulated by its N terminus. *Nucleic Acids Res.* **46**, 3891–3905 (2018).
55. Staudenbauer, W. L. & Orr, E. DNA gyrase: affinity chromatography on novobiocin–Sepharose and catalytic properties. *Nucleic Acids Res.* **9**, 3589–3603 (1981).
56. Lim, K. S. et al. USP1 is required for replication fork protection in BRCA1-deficient tumors. *Mol. Cell* **72**, 925–941 (2018).
57. Liu, J. F. et al. Establishment of patient-derived tumor xenograft models of epithelial ovarian cancer for preclinical evaluation of novel therapeutics. *Clin. Cancer Res.* **23**, 1263–1273 (2017).
58. Harder, E. et al. OPLS3: a force field providing broad coverage of drug-like small molecules and proteins. *J. Chem. Theory Comput.* **12**, 281–296 (2016).
59. Friesner, R. A. et al. Extra precision glide: docking and scoring incorporating a model of hydrophobic enclosure for protein–ligand complexes. *J. Med. Chem.* **49**, 6177–6196 (2006).
60. Knight, J. L. et al. Leveraging data fusion strategies in multireceptor lead optimization MM/GBSA end-point methods. *J. Chem. Theory Comput.* **10**, 3207–3220 (2014).

Acknowledgements

We thank the ICCB-Longwood Screening Facility at Harvard Medical School for their help with small-molecule screening. We thank P. Gokhale and Q. Zeng at the Belfer Center for Applied Cancer Science, as well as C. Yang and K. Parmar at the Center for DNA Damage and Repair, for their help with mouse studies. We thank C. Clairmont for providing RPE1 *BRCA1*$^{-/-}$ cells and purified TRIP13 protein and L. Moreau for her help with chromosome aberration assays. We thank H. Nguyen and S. Spisak for genomic analysis of *POLQ*-knockout clones. We thank C.-L. Tsai at the MD Anderson Cancer Center for providing the BLM-ATPase expression vector. We thank J. Stark for providing DR-GFP and EJ2 repair substrates, and G. Legube for providing DIvA cells for DSB end resection assays. This research was supported by a Stand Up To Cancer (SU2C)–Ovarian Cancer Research Fund Alliance–National Ovarian Cancer Coalition Dream Team Translational Research grant (SU2C-AACR-DT16-15) to A.D.D. SU2C is a program of the Entertainment Industry Foundation. Research grants are administered by the American Association for Cancer Research, the scientific partner of SU2C. This work was also supported by the NIH (grants R37HL052725, P01HL048546, P50CA168504) and the US Department of Defense (grants BM110181 and BC151331P1), as well as grants from the Breast Cancer Research Foundation and the Fanconi Anemia Research Fund to A.D.D. This work was also supported by the Richard and Susan Smith Family Foundation, the Breast Cancer Research Foundation (BCRF-20-033) and the Basser Initiative at the Gray Foundation (167858/167856) (to A.D.D.). This work was also supported by the ERC starting grant (714162) and the Ville de Paris Emergences Program grant (DAE 137) to R.C. This work was also supported by an Ann Schreiber Mentored Investigator Award from the Ovarian Cancer Research Fund Alliance (457527), a Joint Center for Radiation Therapy Award from Harvard Medical School and a Breast & Gynecologic Cancer Innovation Award from the Susan F. Smith Center for Women's Cancers at the DFCI to J.Z. J.A.T. and A.S. are supported by NIH grants P01 CA092548 and R35 CA220430, a Cancer Prevention Research Institute of Texas grant (RP180813) and a Robert A. Welch Chemistry Chair.

Author contributions

J.Z., R.C. and A.D.D. conceived and designed the studies. J.Z., C.G., C.P., A.L., H.Y., R.E.D., A.F., B.K. and A.S. performed experiments and analyzed data. G.I.S., J.A.T., B.S.J.B., R.C. and A.D.D. provided oversight. J.Z., R.C. and A.D.D. prepared the manuscript with input from co-authors.

Competing interests

A.D.D. reports receiving commercial research grants from Eli Lilly and Company, Sierra Oncology and EMD Serono and is a consultant and/or advisory board member for Eli Lilly and Company, Sierra Oncology, Cedilla, Ideaya, Cyteir and EMD Serono. G.I.S. has received research funding from Eli Lilly, Merck KGaA/EMD Serono, Merck and Sierra Oncology, and he has served on advisory boards for Pfizer, Eli Lilly, G1 Therapeutics, Roche, Merck KGaA/EMD Serono, Sierra Oncology, Bicycle Therapeutics, Artios, Fusion Pharmaceuticals, Cybrexa Therapeutics, Astex, Almac, Ipsen, Bayer, Angiex, Daiichi Sankyo, Boehringer Ingelheim, ImmunoMet and Asana. The remaining authors declare no competing interests.

Additional information

Extended data is available for this paper at https://doi.org/10.1038/s43018-021-00203-x.

Supplementary information The online version contains supplementary material available at https://doi.org/10.1038/s43018-021-00203-x.

Correspondence and requests for materials should be addressed to R.C. or A.D.D.

Peer review information *Nature Cancer* thanks Thomas Helleday and the other, anonymous, reviewer(s) for their contribution to the peer review of this work.

Reprints and permissions information is available at www.nature.com/reprints.

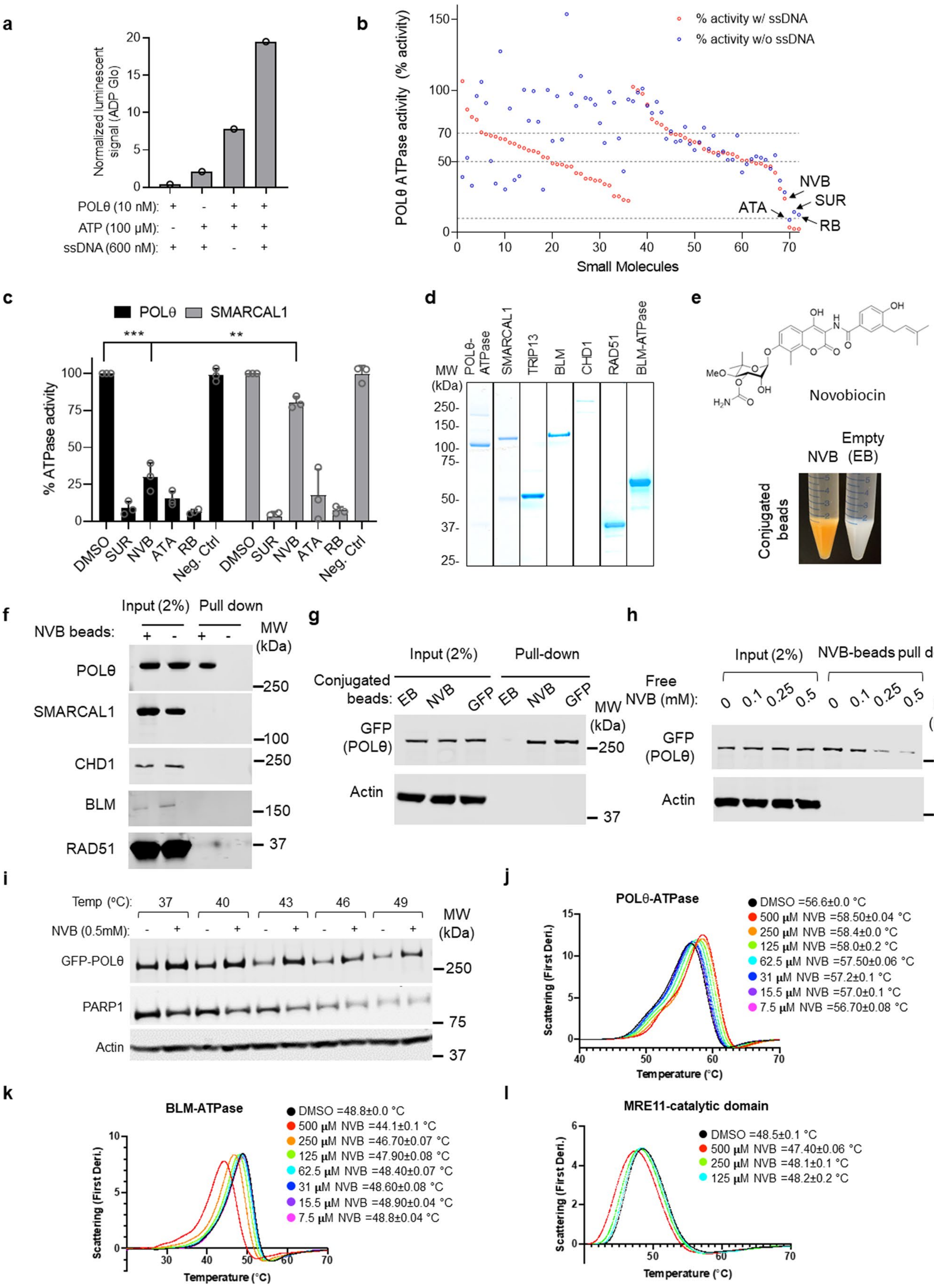

Extended Data Fig. 1 | See next page for caption.

Extended Data Fig. 1 | Characterization of POLθ inhibitors obtained from the small-molecule screen, with biochemical assays and cell-based assays. **a**, ADP-Glo assay for quantification of POLθ ATPase activity in various experimental conditions. N = 1 experiment. **b**, A secondary screen using the 72 initial hits in reducing POLθ ATPase activity (below 70 %, *z*-score < -4). The screen was done in the presence and absence of ssDNA. The four most promising hits advancing for further analysis are labeled (see Table S4 for analysis). Aurintricarboxylic acid (ATA), Reactive Blue 2 (RB), Suramin (SUR), and Novobiocin (NVB). Data shown are mean of n = 2 independent experiments. **c**, Quantification of POLθ and SMARCAL1 ATPase activity with indicated small molecules. The negative control is an inert small molecule (Vandetanib). Data shown are mean ± SD, n = 3 independent experiments. Statistics were performed using two tailed *t*-test with Welch's correction. $***p < 0.001$, $**p < 0.01$. **d**, Coomassie blue stained gels showing purified ATPase that were used in this study. **e**, Conjugation of NVB to epoxy-activated Sepharose-6B (Sigma). NVB conjugated beads showed light yellow color. The structure of NVB is shown. **f**, Pulldown experiments with NVB-conjugated beads and purified POLθ, SMARCAL1, CHD1, BLM, and RAD51. POLθ, SMARCAL1, CHD1, and BLM were detected by Western blot using anti-Flag antibody (Sigma #F1804) in this assay. RAD51 was detected by anti-RAD51 antibody (SantaCruz #398587). **g**, Pulldown experiments with NVB-conjugated beads and cell lysate from HEK293T cells expressing GFP-tagged full-length POLθ. Cell lysates were incubated with empty beads (EB), NVB-beads (NVB) or anti-GFP-beads (GFP) to assay for direct POLθ binding. GFP-POLθ bound to beads and input of each group were subjected to Western blot analysis, using an anti-GFP antibody. **h**, Competition assay between NVB-conjugated beads and free NVB when incubated with GFP-tagged full-length POLθ extracted from HEK293T cells. **i**, Thermal shift assay using GFP-POLQθ expressing HEK293T cell lysate incubated with NVB at the indicated temperatures. Supernatants after heat treatment were subjected to Western blot using anti-GFP and anti-Actin antibodies. **j-l**, Titration of indicated NVB (or DMSO) concentration with POLθ (**j**), BLM (**k**), or MRE11 (**l**) in the thermal shift assay to measure the effect of NVB on the protein stability. Average first derivative of the scattering profile is shown. Scattering peak max values are shown as mean ± SD, from n = 3 independent experiments.

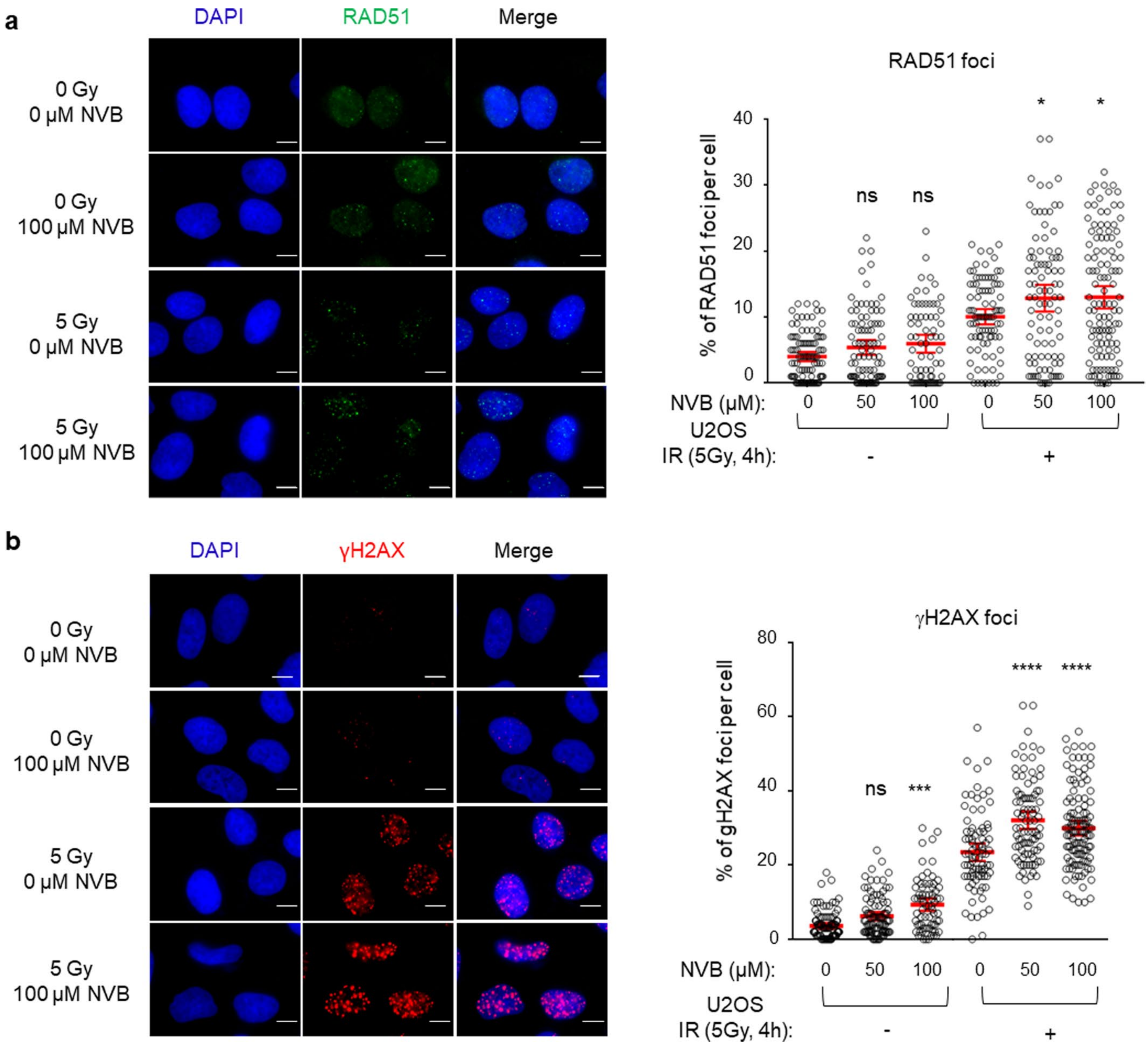

Extended Data Fig. 2 | Novobiocin phenocopies POLθ depletion in human cells. a, Images and quantification of RAD51 foci in U2OS cells under increasing concentrations of NVB with or without gamma-irradiation (IR). **b**, Images and quantification of γH2AX foci in U2OS cells under increasing concentrations of NVB with or without IR. Data in (**a**) and (**b**) were pooled from two independent experiments. Each dot represents foci numbers in one cell. Scale bar = 10 µm.

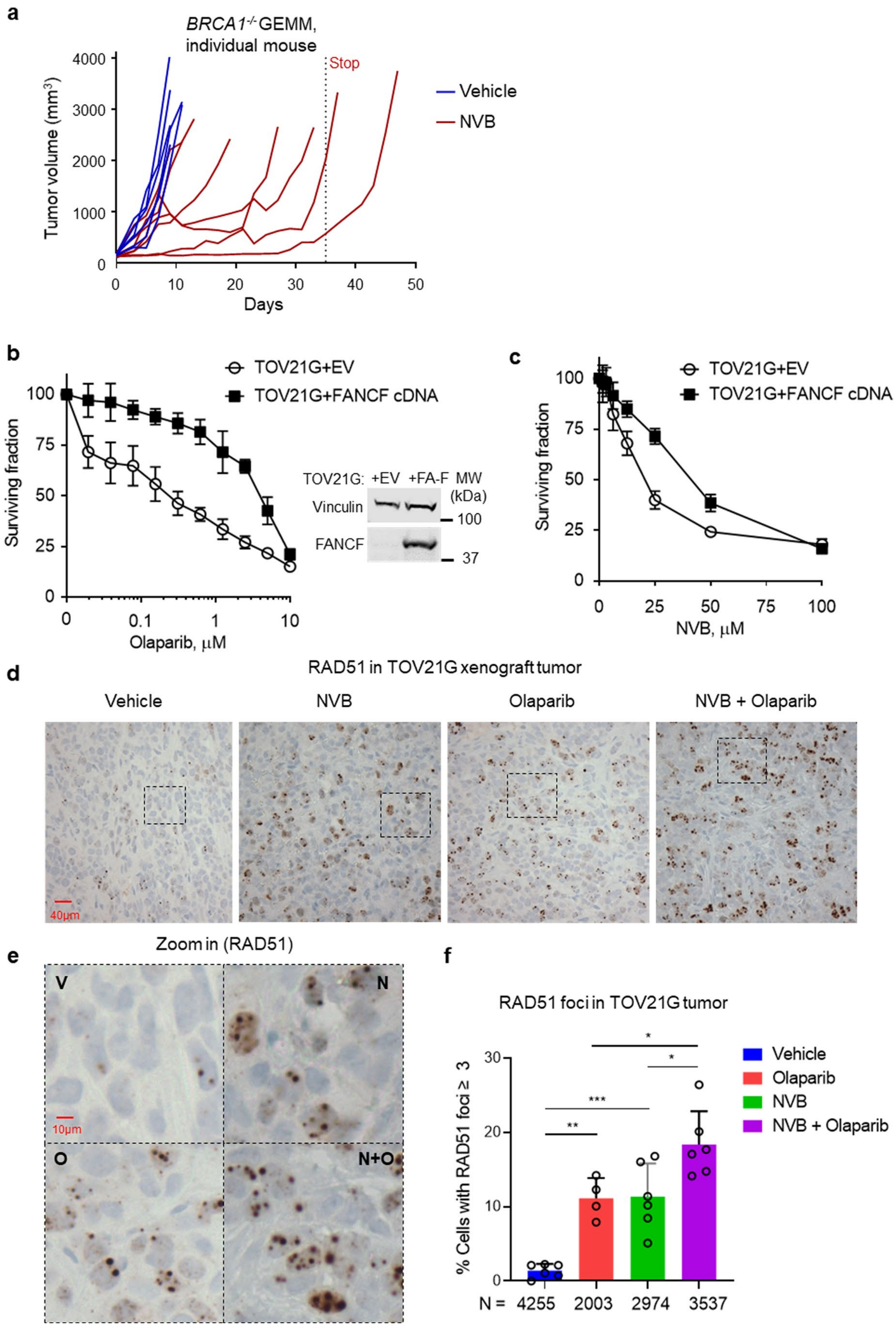

Extended Data Fig. 3 | See next page for caption.

Extended Data Fig. 3 | Efficacy of NVB in *BRCA1*$^{-/-}$ GEMM and RAD51 pharmacodynamic study in TOV21G xenograft models. **a**, NVB efficacy in the GEMM model (*Tp53*$^{-/-}$*Brca1*$^{-/-}$ TNBC). Response of each tumor in each individual mouse is shown. Tumor chunks from GEMM mice were implanted in syngeneic FVB/129P2 mice, which were treated with PBS or 100 mg/kg NVB twice a day via IP for 5 weeks. **b**, Olaparib sensitivity of TOV21G (+ EV) or FANCF-complemented TOV21G (+ FANCF cDNA). **c**, Novobiocin sensitivity of TOV21G (+ EV) or FANCF-complemented TOV21G (+ FANCF cDNA). Mean ± SD of n = 6 biologically independent samples are shown in **b** and **c**. **d-f**, Immunohistochemical (IHC) study of the pharmacodynamic biomarker RAD51 after NVB and/or olaparib treatment in TOV21G tumors. **d**, Representative images of RAD51 IHC staining in xenografted TOV21G tumor cells. Tumor bearing NU(NCr)-Foxn1nu mice were treated with indicated drugs for 18 days before tumors were taken. FFPE tissue sections of the tumors were stained using an anti-RAD51 antibody and representative images (40X) are shown. **e**, Zoom-in of the IHC images in (**d**) to show RAD51 foci in detail. **f**, Quantification of RAD51 foci positive cells in TOV21G tumors. Cells with three or more RAD51 foci were counted as positive cells. Tumor samples from each group were processed and analyzed, and Mean±SD are shown, n = 4 for Olaparib and n = 6 for other groups. The total number of cells counted were shown in the graph (N). Statistical analysis was performed using one-way ANOVA in Prism, *, $p < 0.05$; **, $p < 0.01$; ***, $p < 0.001$.

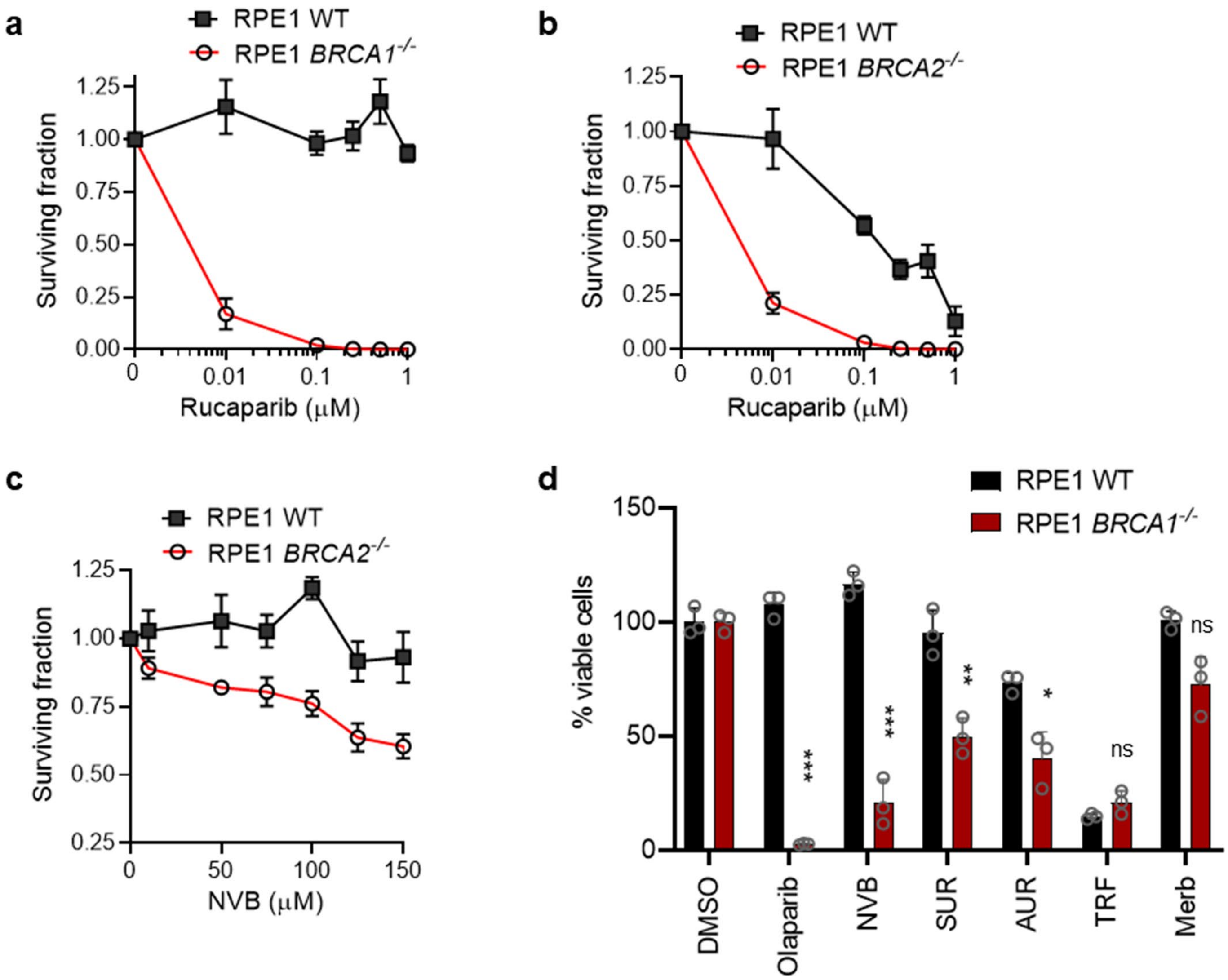

Extended Data Fig. 4 | Effects of novobiocin in *BRCA1*$^{-/-}$ and *BRCA2*$^{-/-}$ cells. a, Clonogenic survival of *BRCA1*$^{-/-}$ and WT RPE1 cells under increasing concentrations of the PARPi rucaparib. **b**, Clonogenic survival of *BRCA2*$^{-/-}$ and WT RPE1 cells under increasing concentrations of PARPi rucaparib. **c**, Clonogenic survival of *BRCA2*$^{-/-}$ and WT RPE1 cells under increasing concentrations of POLθ inhibitor. The survival fraction in **a-c** is normalized to the untreated samples. Data shown are Mean ± SEM, n = 3 independent experiments. **d**, Cell viability assay (CellTiter-Glo) in *BRCA1*$^{-/-}$ and WT RPE1 cells treated with indicated POLθ inhibitors (50 μM) or with the PARPi Olaparib as control. Cells were treated twice on days 1 and 4 and cell viability was measured on day 7. Data were mean ± SD, n = 3 biological replicates. Statistics analyses were two tailed *t*-test. *, $p < 0.05$; **, $p < 0.01$; ***, $p < 0.001$, ns, not significant ($p > 0.05$).

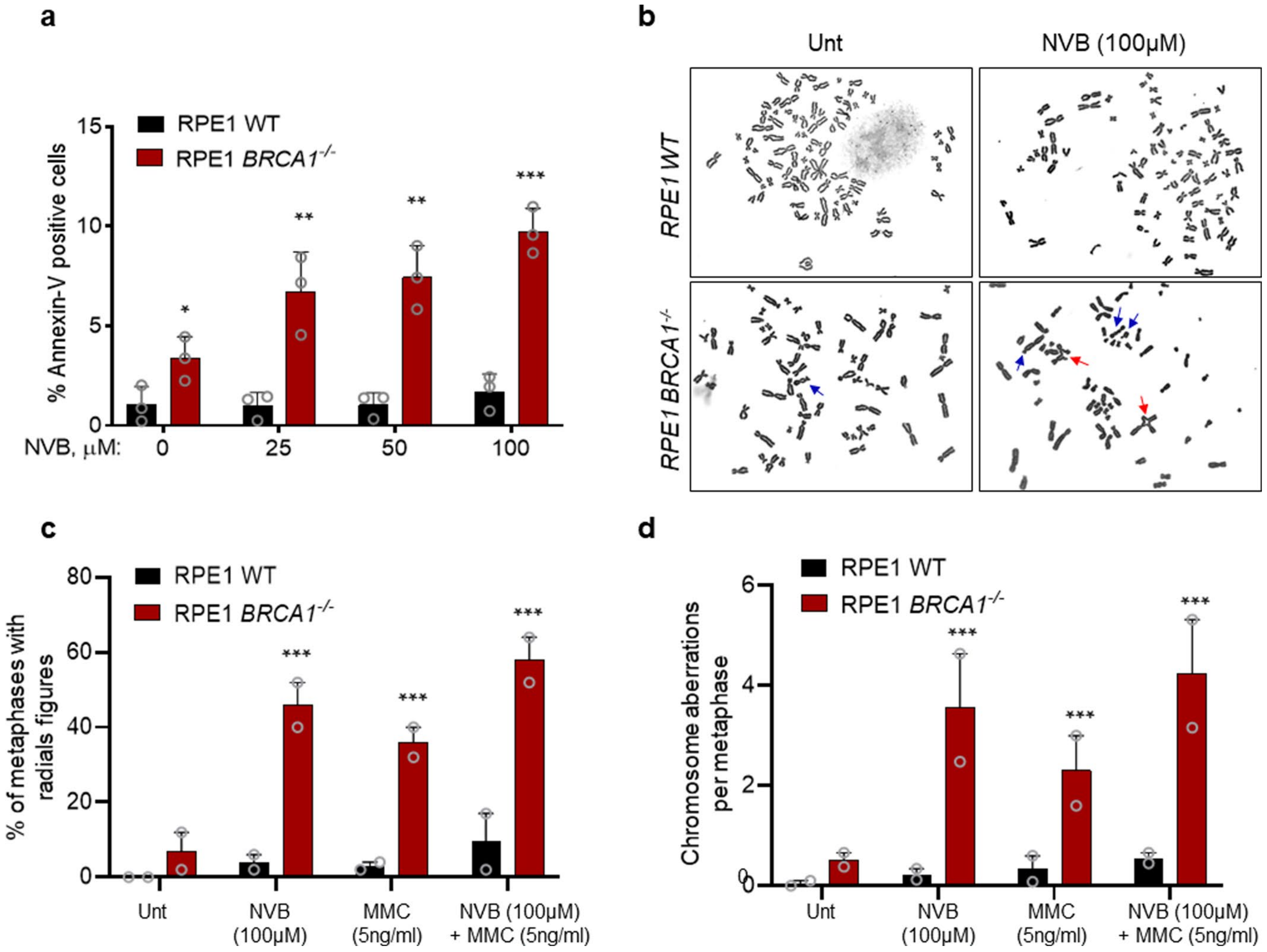

Extended Data Fig. 5 | NVB induces apoptosis and chromosome aberrations in *RPE1 BRCA1*$^{-/-}$. **a**, Quantification of apoptosis in *BRCA1*$^{-/-}$ and WT RPE1 cells under increasing concentrations of NVB. Mean ± SD, n = 3 independent experiments. **b**, Representative images of chromosomal aberrations (blue arrows) including radial figures (red arrows) in RPE1 (WT or *BRCA1*$^{-/-}$) cells treated with NVB. **c-d**, Quantification of radial figures (**c**) and total chromosome aberration (**d**) in *BRCA1*$^{-/-}$ and WT RPE1 cells treated with NVB alone or in combination with mitomycin C (MMC). Data in **c-d** are mean ± SD of n = 3 independent experiments. Statistical significance was determined by one-way ANOVA multiple comparisons using uncorrected Fisher's LSD test. ***, $p < 0.001$.

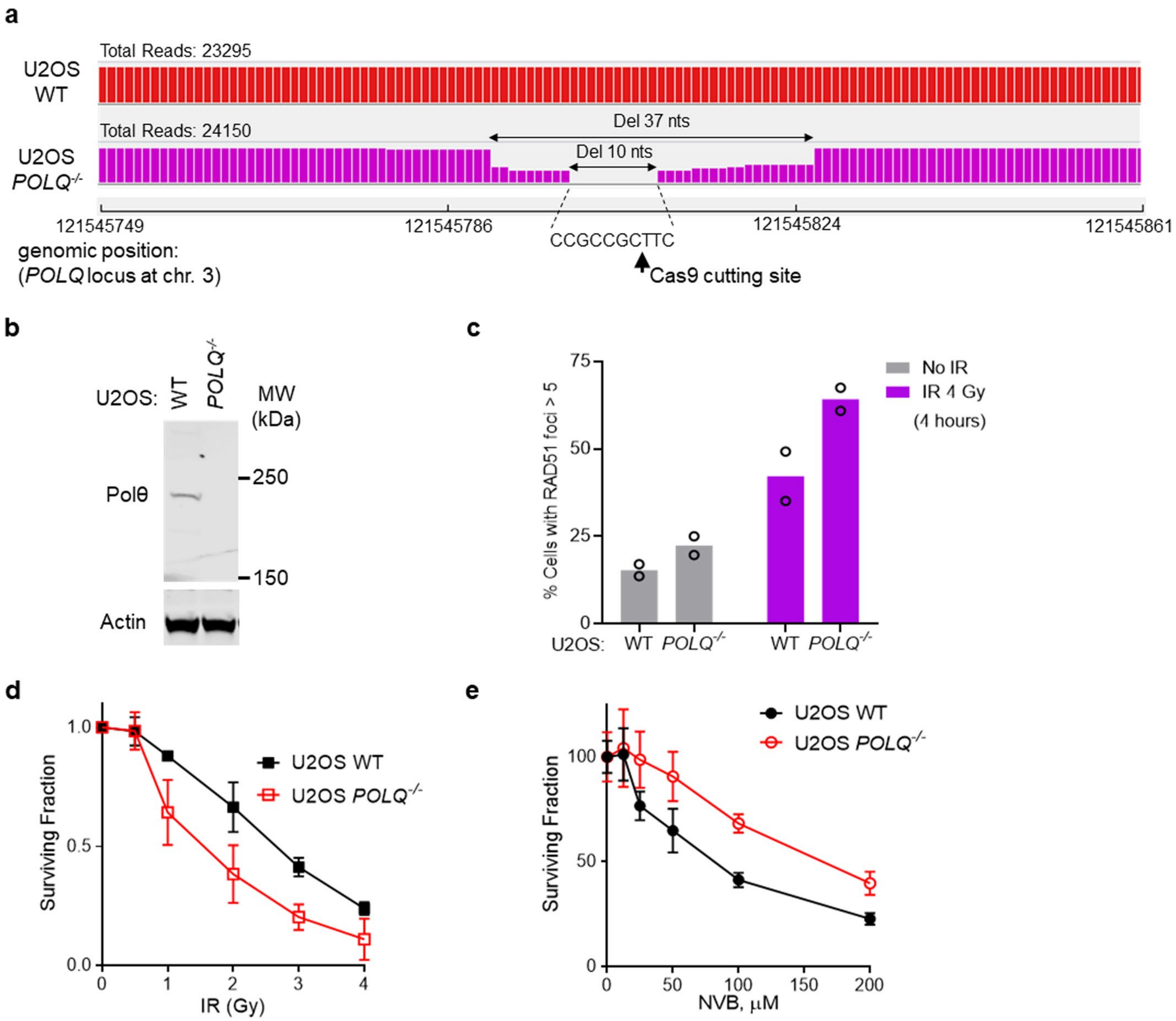

Extended Data Fig. 6 | *POLQ*$^{-/-}$ U2OS cells were resistant to NVB. a–d, Verification of the U2OS-*POLQ*$^{-/-}$ cell line. **a**, Mapping the genetic alteration (deletions) in the U2OS *POLQ* knockout clone generated by CRISPR-Cas9. The targeted region was sequenced by Next Gen sequencing (number of reads are shown), and the deletions were mapped to *POLQ* locus of human genome on chromosome 3. **b**, A Western blot showing POLθ protein expression in WT and *POLQ*$^{-/-}$ U2OS cells. **c**, RAD51 foci assay in WT or *POLQ*$^{-/-}$ U2OS cells before and after (4 h) of 4 Gy IR. Mean of n = 2 independent experiments is shown. **d**, IR sensitivity of WT and *POLQ*$^{-/-}$ U2OS cells in clonogenic assays. Mean ± SD of n = 3 independent experiments are shown. **e**, NVB sensitivity of WT and *POLQ*$^{-/-}$ U2OS cells in clonogenic assays. Mean ± SD of n = 6 biologically independent samples are shown.

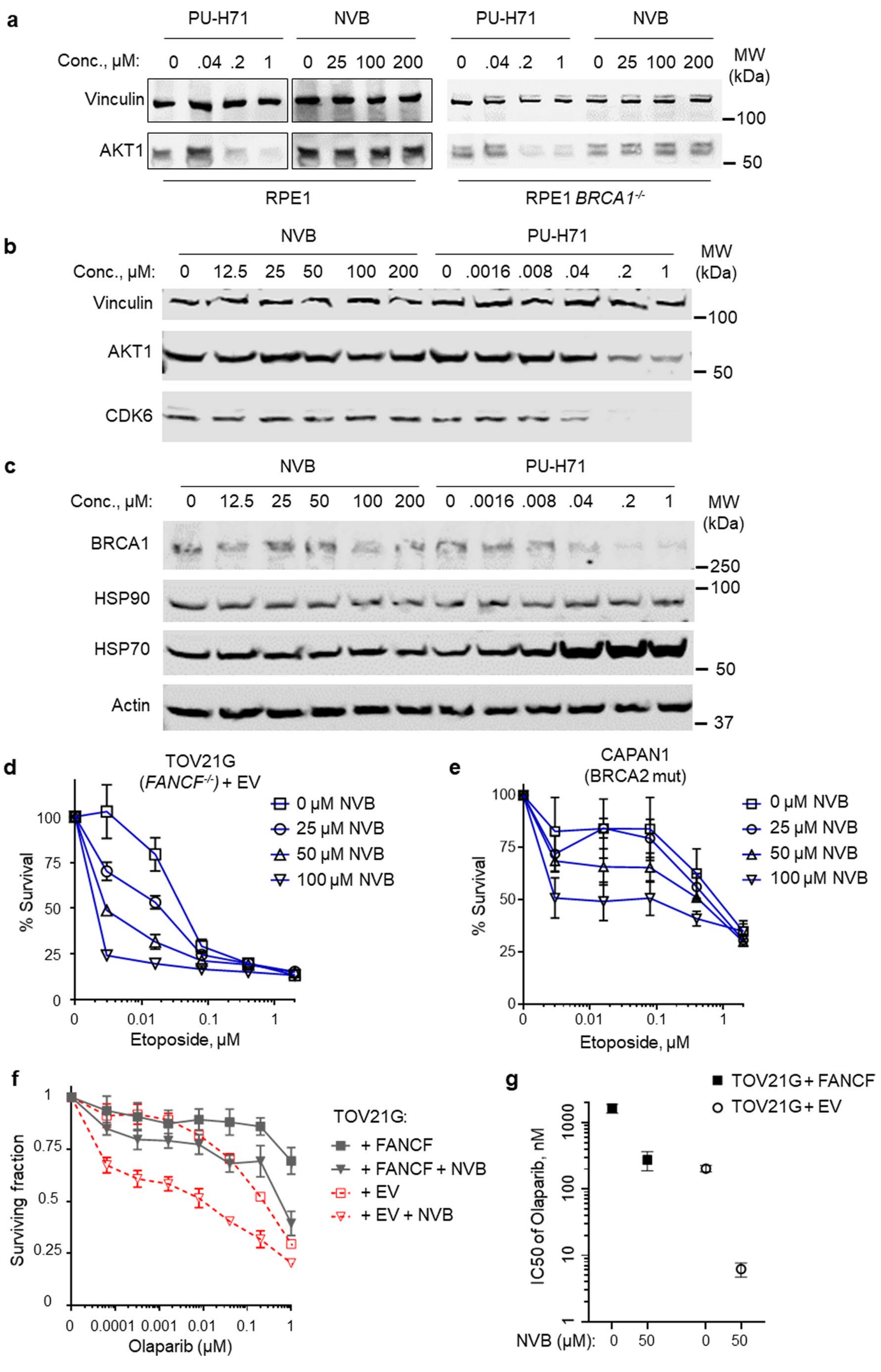

Extended Data Fig. 7 | See next page for caption.

Extended Data Fig. 7 | NVB inhibits POLθ but not HSP90 or TOP2 in human cells. a, HSP90 client degradation assay in RPE1 and RPE1-*BRCA1*$^{-/-}$ cells. Cells were treated with a potent HSP90 inhibitor PU-H71 or NVB for 48 hours, and then cells were collected for Western blot analysis of the HSP90 client AKT1. **b-c**, HSP90 client degradation assay in MCF7 cells. Cells were treated with the potent HSP90 inhibitor PU-H71 or NVB for 24 hours, and then cells were collected for Western blot analysis of the HSP90 client proteins AKT1, CDK6 (**b**) and BRCA1 (**c**). Levels of HSP90 and HSP70 were also analyzed after NVB or PU-H71 treatment (**c**). **d-e**, Combination effect of etoposide and novobiocin in killing TOV21G cells (**d**) and CAPAN1 cells (**e**), showing their non-epistatic effects. Mean ± SD of n = 3 independent experiments are shown. **f**, CellTiter-Glo cell viability assay of empty vector (EV) and FANCF-complemented TOV21G cells, in the presence of olaparib, novobiocin or both. Mean ± SD, n = 4 biological replicates are shown. **g**, IC_{50} values of olaparib in TOV21G cells with or without NVB, derived from data in **f**. Mean ± SD of IC_{50} were shown, from n = 4 biological replicates.

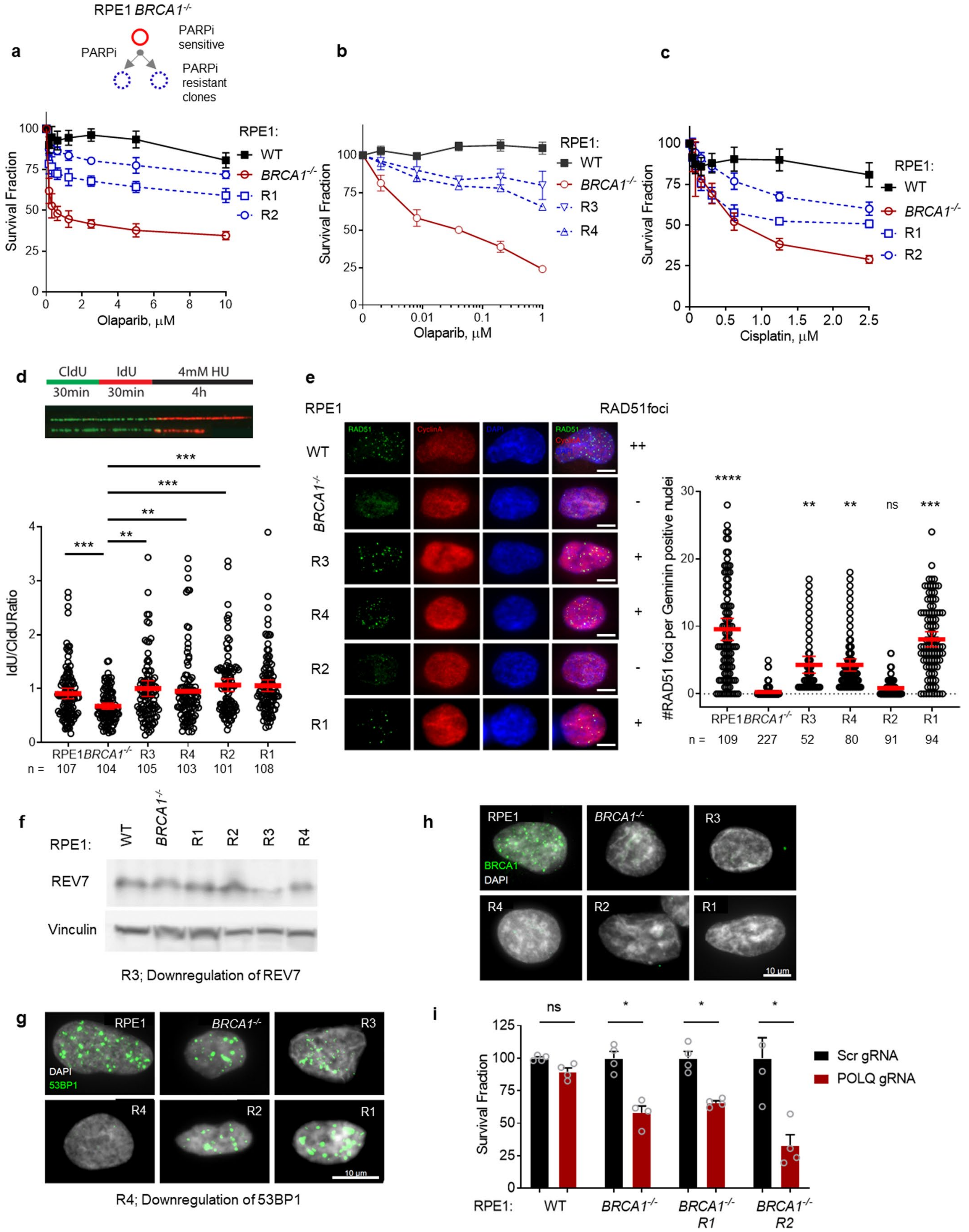

Extended Data Fig. 8 | See next page for caption.

Extended Data Fig. 8 | Characterization of PARP inhibitor resistant clones derived from RPE1-*BRCA1*$^{-/-}$. a–c, Olaparib (**a-b**) and cisplatin (**c**) sensitivity of WT and *BRCA1*$^{-/-}$ RPE1 cells and the PARPi resistant clones of *BRCA1*$^{-/-}$ RPE1. Mean ± SD of biological replicates are shown, with n = 8 in **A**, n = 3 in **B**, and n = 8 in **C**. **d**, DNA fiber assay to measure the replication fork stability of the PARPi resistant clones. Mean±95%CI are shown from 3 independent experiments are shown, with n = number of fibers scored labeled. **e**, RAD51 foci analysis in WT and *BRCA1*$^{-/-}$ RPE1 cells and the PARPi resistant clones after irradiation (5Gy), to determine restoration of RAD51 foci in R clones. RAD51 was stained 4 hours after IR. Scale bar = 10 µm. **f**, A Western blot of WT and *BRCA1*$^{-/-}$ RPE cells and the PARPi resistant clones using a REV7 antibody. **g**, Immunofluorescence staining of 53BP1 in WT and *BRCA1*$^{-/-}$ RPE1 cells and the PARPi resistant clones after irradiation. Clone R4 showed much reduced 53BP1 foci after IR. **h**, Immunofluorescence staining of BRCA1 in WT and *BRCA1*$^{-/-}$ RPE1 cells and the PARPi resistant clones after irradiation. No BRCA1 foci was observed except in WT RPE1 cells. **i**, CellTiter-Glo assay to determine survival of PARPi-resistant and parental *BRCA1*$^{-/-}$ RPE1 cells upon CRISPR knockout of the *POLQ* gene. Data are mean ± SEM, with n = 4 biological replicates. Statistical analysis was *t*-test, *, $p < 0.05$; ns, not significant.

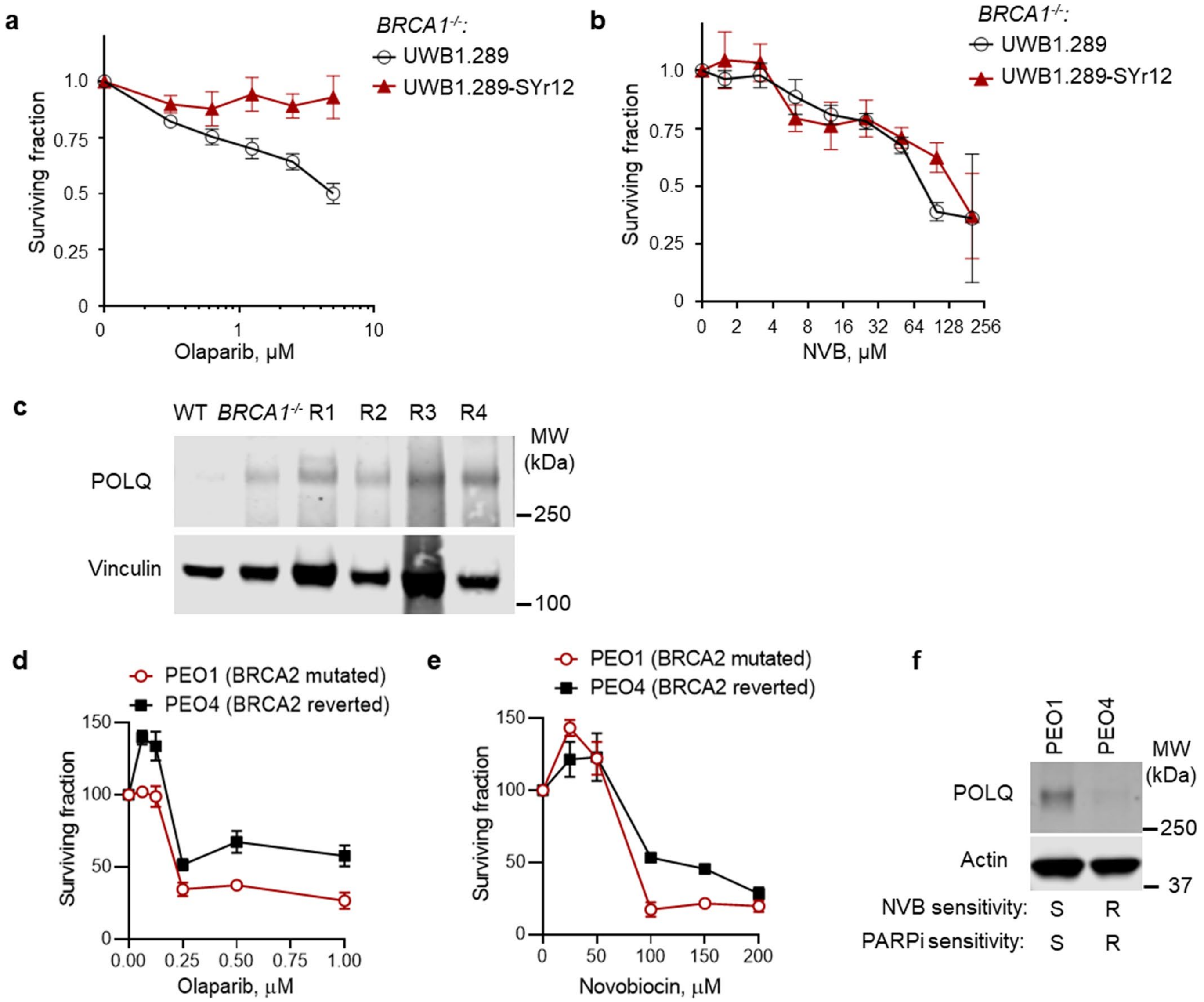

Extended Data Fig. 9 | PARPi resistant MDA-MB-436 and UWB1.289 cells are sensitive to NVB, and NVB has synergy with PARPi in TOV21G cells. **a-b**, Olaparib (**a**) and NVB (**b**) sensitivity of UWB1.289 and a PARPi resistant UWB1.289 clone (UWB1.289-YSR12) in CellTiter-Glo assays. Data shown are mean ± SD, n = 4 biological replicates. **c**, Western blot analysis of POLQ expression levels in in WT and *BRCA1*$^{-/-}$ RPE1 cells and the PARPi resistant *BRCA1*$^{-/-}$ clones. **d**, Olaparib sensitivity of PEO1 (BRCA2 mutated) and PEO4 cells (BRCA2 restored). **e**, NVB sensitivity of PEO1 and PEO4 cells. Data shown in **d** and **e** are Mean ± SD, n = 3 biological replicates. **f**, A Western blot shows POLQ expression in BRCA2-deficient cells lines (PEO1) and their counterparts with BRCA2 reverted to wild type (PEO4).

nature research

Corresponding author(s): Alan D'Andrea

Last updated by author(s): Mar 8, 2021

Reporting Summary

Nature Research wishes to improve the reproducibility of the work that we publish. This form provides structure for consistency and transparency in reporting. For further information on Nature Research policies, see our Editorial Policies and the Editorial Policy Checklist.

Statistics

For all statistical analyses, confirm that the following items are present in the figure legend, table legend, main text, or Methods section.

n/a	Confirmed	
☐	☒	The exact sample size (*n*) for each experimental group/condition, given as a discrete number and unit of measurement
☐	☒	A statement on whether measurements were taken from distinct samples or whether the same sample was measured repeatedly
☐	☒	The statistical test(s) used AND whether they are one- or two-sided *Only common tests should be described solely by name; describe more complex techniques in the Methods section.*
☒	☐	A description of all covariates tested
☐	☒	A description of any assumptions or corrections, such as tests of normality and adjustment for multiple comparisons
☐	☒	A full description of the statistical parameters including central tendency (e.g. means) or other basic estimates (e.g. regression coefficient) AND variation (e.g. standard deviation) or associated estimates of uncertainty (e.g. confidence intervals)
☐	☒	For null hypothesis testing, the test statistic (e.g. *F*, *t*, *r*) with confidence intervals, effect sizes, degrees of freedom and *P* value noted *Give P values as exact values whenever suitable.*
☐	☒	For Bayesian analysis, information on the choice of priors and Markov chain Monte Carlo settings
☐	☒	For hierarchical and complex designs, identification of the appropriate level for tests and full reporting of outcomes
☐	☒	Estimates of effect sizes (e.g. Cohen's *d*, Pearson's *r*), indicating how they were calculated

Our web collection on statistics for biologists contains articles on many of the points above.

Software and code

Policy information about availability of computer code

Data collection	IVIS-200 Bioluminescent System (Xenogen), Odyssey Infrared Imagers (Li-Cor), Zeiss PALMRobo V4.6, QuantStudio 7 Flex Real-Time PCR Systems, SpectraMax M5.
Data analysis	GraphPad Prism 8.2.1, ImageJ 1.52n, Image Studio Lite version 5.2.5 (Li-Cor), Xenogen IVIS-200 Bioluminescent System, QuantStudio 7 Flex, Zen 3.1 (blue edition), Excel (Microsoft 365 MSO v16.0.13127.21210), SoftMax Pro 6.5.

For manuscripts utilizing custom algorithms or software that are central to the research but not yet described in published literature, software must be made available to editors and reviewers. We strongly encourage code deposition in a community repository (e.g. GitHub). See the Nature Research guidelines for submitting code & software for further information.

Data

Policy information about availability of data

All manuscripts must include a data availability statement. This statement should provide the following information, where applicable:

- Accession codes, unique identifiers, or web links for publicly available datasets
- A list of figures that have associated raw data
- A description of any restrictions on data availability

All data associated with the paper are reported. Raw data/images are provided in Table S5 and Figure S10.

Field-specific reporting

Please select the one below that is the best fit for your research. If you are not sure, read the appropriate sections before making your selection.

☒ Life sciences ☐ Behavioural & social sciences ☐ Ecological, evolutionary & environmental sciences

For a reference copy of the document with all sections, see nature.com/documents/nr-reporting-summary-flat.pdf

Life sciences study design

All studies must disclose on these points even when the disclosure is negative.

Sample size	No statistical methods were used to determine sample size. Sample size info is provided in figure legends for each experiment. More than three samples were used whenever possible. For in vivo mouse studies, we use at least 6 mice per group, to ensure statistical strength.
Data exclusions	No data was excluded from analyses.
Replication	We have verified all of our results in at least two independent experiments. Replication info was provided in the Figure legends for experiment. Raw data are provided in Table S5.
Randomization	For mouse studies, mice were randomized according to their initial tumor sizes so that each treatment group had approximately equal initial average tumor size. For other studies, no randomization method was used.
Blinding	The person who carried the mouse xenograft studies were blinded with the identities of the tumor cells being xenografted and treated. The person who carried the PDX studies were blinded with the genotypes of the tumors being studied. For other studies, no specific blinding method was used.

Reporting for specific materials, systems and methods

We require information from authors about some types of materials, experimental systems and methods used in many studies. Here, indicate whether each material, system or method listed is relevant to your study. If you are not sure if a list item applies to your research, read the appropriate section before selecting a response.

Materials & experimental systems

n/a	Involved in the study
☐	☒ Antibodies
☐	☒ Eukaryotic cell lines
☒	☐ Palaeontology and archaeology
☐	☒ Animals and other organisms
☒	☐ Human research participants
☒	☐ Clinical data
☒	☐ Dual use research of concern

Methods

n/a	Involved in the study
☒	☐ ChIP-seq
☒	☐ Flow cytometry
☒	☐ MRI-based neuroimaging

Antibodies

Antibodies used	BRCA1 antibody (Millipore #OP92) BRCA2 (Cell Signaling Technology #1074) POLθ (Sigma #SAB1402530) β-Actin (Cell Signaling Technology #3700) γH2AX (Millipore #05-636) RAD51 (Santa Cruz Biotechnology, SCB, #sc-8349) RAD51 (Cell Signaling Technology #8875) CDK6 (SCB #sc-7961) AKT1 (SCB #sc-5298) HSP70 (SCB #sc-24) HSP90 (SCB #sc-13119) Vinculin (SCB # sc-25336) FANCF (Everest Biotech, #EB06112) Goat anti-Rabbit Secondary Antibody, Alexa-488 (Life Technologies A11034) Goat anti-mouse Secondary Antibody, Alexa-594 (Life Technologies A11005)
Validation	Results using the antibodies were shown in the current manuscript.

Eukaryotic cell lines

Policy information about cell lines

Cell line source(s)	SF9 cells (ThermoFisher) U2OS (ATCC), RPE1 (ATCC), MDA-MB-436 (ATCC), UWB1.289 (Zou lab), U2OS-DRGFP (Stark lab), U2OS-EJ2 (Stark lab), TOV21G (ATCC), 293T (ATCC), CAPAN1 (ATCC). Gene modified strains such as RPE1-BRCA1-/-, RPE1-BRCA2-/- and, RPE1-POLQ-/-, and U2OS-POLQ-/- were generated in the D'Andrea and Ceccaldi labs except specified otherwise in the manuscript.
Authentication	We did not authenticated our cell lines individually in the lab.
Mycoplasma contamination	All cell lines used have been tested negative for mycoplasma in the lab. MDA-MB-436 lines, TOV21G lines, and RPE1 lines, and CAPAN1 cells have been tested negative for mycoplasma by Charles Rivers.
Commonly misidentified lines (See ICLAC register)	NA

Animals and other organisms

Policy information about studies involving animals; ARRIVE guidelines recommended for reporting animal research

Laboratory animals	Female NU(NCr)-Foxn1nu athymic nude mice, older than 6 week at time of experiments. Female FVB/129P2 mice, at least 6 week at time of experiments. Female NSG mice, 8 week at time of experiments.
Wild animals	No wild animals were used in the study.
Field-collected samples	No field collected samples were used in the study.
Ethics oversight	Institutional Review Boards (IRBs) and the Animal Care and Use Committee (ACUC), Dana-Farber Cancer Institute. All animal experiments were conducted in accordance with Institutional Animal Care and Use Committee-approved protocols at Beth Israel Deaconess Medical Center and Dana-Farber Cancer Institute

Note that full information on the approval of the study protocol must also be provided in the manuscript.